

**NASA CONTRACTOR  
REPORT**

**NASA CR-206**



**NASA CR-206**

0099759



**ON THE USE OF MAGNETOHYDRODYNAMICS  
DURING HIGH SPEED RE-ENTRY**

*by P. O. Jarvinen*

Prepared under Contract No. NASw-748 by  
**AVCO-EVERETT RESEARCH LABORATORY**  
Everett, Mass.

*for*

**NATIONAL AERONAUTICS AND SPACE ADMINISTRATION • WASHINGTON, D. C. • APRIL 1965**



ON THE USE OF MAGNETOHYDRODYNAMICS  
DURING HIGH SPEED RE-ENTRY

By P. O. Jarvinen

Distribution of this report is provided in the interest of information exchange. Responsibility for the contents resides in the author or organization that prepared it.

Prepared under Contract No. NASw-748 by  
AVCO-EVERETT RESEARCH LABORATORY  
Everett, Mass.

for

NATIONAL AERONAUTICS AND SPACE ADMINISTRATION

---

For sale by the Office of Technical Services, Department of Commerce,  
Washington, D.C. 20230 -- Price \$3.00



## ABSTRACT

The use of the interaction of a magnetic field with a hypersonic flow, to effect the decelerations and heating encountered during re-entry is considered. The equations of motion which describe the re-entry history of non-lifting vehicles employing magnetohydrodynamic interactions with the flow field are simplified in the manner of Allen and Eggers. Analytical expressions are derived for the velocity history, deceleration history, and the altitude and magnitude of peak heating and deceleration for re-entries involving both low or high magnetic Reynolds number interactions. In both cases it is found that the maximum heating and deceleration experienced can be reduced significantly below that encountered by purely aerodynamic vehicles.

Vertical re-entries at velocities of 40,000 and 50,000 ft per second are considered. Solutions for the trajectories require the use of high magnetic Reynolds number theory initially with transition to low magnetic Reynolds number theory when both theories predict equivalent drag areas. The drag area predicted by the low magnetic Reynolds number theory decreases more rapidly with altitude than that predicted on the basis of high magnetic Reynolds number. This reduces the maximum decelerations encountered below the values predicted by the purely high magnetic Reynolds number theory. A reduction in peak deceleration of about 35 percent was achieved due to the magnetohydrodynamic interaction. Significant reductions in heating were also achieved.

A comparative study of magnetohydrodynamic and aerodynamic vehicles was performed for lifting re-entries with lift to drag ratios from  $1/2$  to 4, typical of manned return from Mars or Venus. Use of magnetohydrodynamic interaction significantly widens the re-entry corridor and decreases the re-entry heating. On the undershoot boundary the heat load experienced by the magnetohydrodynamic vehicle is one order of magnitude less than that of the aerodynamic vehicle while on the overshoot boundary, it is two orders of magnitude less. It was found that in general, estimated weights of the magnetic coils needed to produce the magnetohydrodynamic interaction were considerably smaller than the heat protection weight required without the magnetic field.



## TABLE OF CONTENTS

SECTION	Page
Abstract	iii
Nomenclature	vii
I. Introduction	1
II. Re-entry Dynamics of MHD Vehicles	3
A. Re-entry at Low Magnetic Reynolds Number	3
B. Re-entry at High Magnetic Reynolds Number	7
III. Vertical Re-entry	11
A. Dynamics	11
B. Heating	13
IV. Lifting Re-entry	21
APPENDICES	
A. Emissivity of Low $R_M$ Gas Volume	43
B. Cylindrical Approximation to Low $R_M$ Gas Volume	49
C. Emissivity of Hemispherical Shell Volume	51
D. Radiation Heating Model for Aerodynamic Vehicle	53
References	61



## NOMENCLATURE

a	frequency averaged absorption coefficient
A	reference area
b	radius of magnetic coil
B	magnetic field strength
$C_D$	drag coefficient
D	drag
e	electronic charge
g	acceleration of gravity
g's	deceleration with reference to acceleration of gravity
I	current
i	current density
m	magnetic moment of coil
$m_B$	mass of re-entry body
$M_C$	mass of magnetic coil
$N_e$	number of electrons per cubic meter
R	radius of shock
$R_M$	magnetic Reynolds number $\sigma \mu_o V \epsilon R$
t	time
v	velocity
w	weight of re-entry vehicle
x	horizontal distance
y	altitude

$\omega_T$	Hall coefficient $\sigma B/N_e e$
$\beta$	inverse scale height of atmosphere
$\epsilon$	density ratio across the shock wave $\rho_\infty/\rho_1$
$\theta$	flight path angle with respect to local horizontal
$\rho$	density
$\sigma$	electrical conductivity of ionized gas
$\mu_0$	permeability of free space

### Subscripts

E	initial re-entry conditions
1	flow property directly behind normal shock
0	sea level property
$\infty$	free stream property
Max G	conditions at maximum deceleration
Max $\dot{q}_{rad}$	conditions at maximum radiation heating

## SECTION I

### INTRODUCTION

The application of magnetohydrodynamics to high speed flight has been considered by Kantrowitz<sup>1</sup>. It has been proposed that MHD may be used to increase drag, to produce lift forces or control moments, to generate electrical power or to reduce heat transfer during re-entry.

Unfortunately, it was usually found that the advantage gained through magnetohydrodynamic interaction was more than compensated by the joule dissipation in the coil required to create the MHD effect. Consequently, flight applications of MHD have not been found too practical.

The recent advances in superconductivity and the promise of the availability of large superconducting magnets may change this situation. If the strong and large magnetic fields can be maintained essentially without joule dissipation, many of the previously discarded ideas become attractive.

Motivated by these advances, a number of theories concerning the interaction of a magnetic field with hypersonic flows have recently appeared in the literature. Levy and Petschek<sup>2</sup> considered the hypersonic flow about the magnetic field of a long current carrying wire for both high and low magnetic Reynolds number. Locke, Petschek and Rose<sup>3</sup> reported experimental results which demonstrated the general characteristics indicated by this theory. Levy<sup>4</sup> considered the interaction of high magnetic Reynolds number hypersonic flow with the magnetic field of a two-dimensional dipole. Levy, Gierasch and Henderson<sup>5</sup> considered low magnetic Reynolds number hypersonic flow past either a two- or three-dimensional magnetic dipole with its axis oriented parallel to the flow.

In this paper, we have utilized the above theoretical analyses to evaluate the potential of magnetohydrodynamic interactions with the flow about high speed re-entry vehicles. As typical examples, we consider the entry of a 1000 pound probe, say, returning soil or photographic samples, from a Martian mission at 40,000 or 50,000 ft/sec entry velocity and the entry of a 10,000 pound manned vehicle at 40,000 ft/sec velocity. The MHD effects on the trajectory, forces, and resultant heating rates are calculated in the following sections.



## SECTION II

### RE-ENTRY DYNAMICS OF MHD VEHICLES

#### A. Re-entry at Low Magnetic Reynolds Number

In this section, a simplified analysis of the trajectory of a non-lifting vehicle employing MHD during entry into the earth's atmosphere is presented for the case of low magnetic Reynolds number, i. e.,  $RM \ll 1$ . The vehicle is assumed to be axially symmetric and to contain a magnetic dipole with its axis oriented parallel to the flow.

The equations of motion\* for a body of mass  $m$ , with speed  $v$ , at an altitude  $y$  and an angle of approach  $\theta$  to the horizontal are:

$$\frac{d^2 y}{dt^2} = -g + \frac{C_D \rho V^2 A}{2 m_B} \sin \theta \quad (1)$$

and

$$\frac{d^2 x}{dt^2} = \frac{C_D \rho V^2 A}{2 m_B} \cos \theta \quad (2)$$

Where the drag coefficient is

$$C_D = \frac{2 D}{\rho V^2 A} \quad (3)$$

These equations can be simplified further as in Allen and Eggers<sup>6</sup>, by assuming that

1. The drag coefficient is constant
2. The flight path is a straight line inclined at angle  $\theta_E$  to horizontal.
3. The gravity term in Eq. (1) can be neglected provided the angle to the horizontal is not too small.
4. The density as a function of altitude is given by the relation  $\rho = \rho_0 e^{-\beta y}$ .

---

\* Assuming flight over a flat earth.

Equations (1) and (2) may then be re-written as

$$\frac{d^2 y}{d t^2} = \frac{C_D \xi V^2 A}{2 m_B} \sin \Theta_E \quad (4)$$

and

$$\frac{d^2 x}{d t^2} = \frac{C_D \xi V^2 A}{2 m_B} \cos \Theta_E \quad (5)$$

To account for the magnetic interaction we now take the resultant deceleration equation as

$$-\frac{dV}{dt} = \frac{C_D \xi V^2 \pi R^2}{2 m_B} \quad (6)$$

with R the radius of the shock, determined by the interaction of the magnetic field with the ionized gas. For low magnetic Reynolds number ( $R_M \leq 1.0$ ), the theory of Levy<sup>5</sup> for a hypersonic flow about a magnetic dipole is used to determine the radius of the shock. The resulting condition is that the interaction parameter, S the ratio of that magnetic force per unit area to the dynamic pressure,  $\epsilon R$ , is unity, i. e.

$$S = \frac{\epsilon \sigma B^2 R}{\xi V} = 1.0 \quad (7)$$

The magnetic field strength is that given by the far field of a single loop of current-carrying wire, i. e.

$$B = \frac{m}{2 \pi R^3} \quad (8)$$

where m is the magnetic moment defined as

$$m = \mu_0 I A = \mu_0 I \pi b^2$$

If Eq. (8) is substituted into Eq. (7), the radius of the shock becomes

$$R = \left( \frac{\epsilon \sigma m^2}{\xi V 4 \pi^2} \right)^{1/5} \quad (9)$$

and the drag area of the shock is

$$A = \pi R^2 = \pi \left( \frac{\epsilon \sigma m^2}{\xi V 4 \pi^2} \right)^{2/5} \quad (10)$$

The electrical conductivity of ionized air directly behind a normal shock, assuming thermochemical equilibrium to exist, is shown in Fig. 1. In the analytical treatment to follow, it is assumed that the electrical conductivity of ionized air may be approximated by the following expression

$$\sigma = \sigma_0 \left( \frac{V}{V_E} \right)^N \quad (11)$$

where

$$\sigma_0 = A (V_E)^N \quad (12)$$

The approximation to the conductivity used is noted in Fig. 1 and is given by the equation

$$\sigma = 7.77 \times 10^{-18} (V_E)^{5.14} \left( \frac{V}{V_E} \right)^{5.14} \quad (13)$$

where  $\sigma$  is in mhos/meter and  $V_E$  in meters/sec. The electrical conductivity given by Eq. (13) is in better agreement with the actual conductivity at lower altitudes. This is desirable since most of the contribution to the total MHD effect occurs at or near peak deceleration. For very high speed vertical re-entries peak deceleration occurs at altitudes below 150,000 feet.

For a straight line trajectory<sup>6</sup>

$$\frac{dY}{dt} = -V \sin \theta_E \quad (14)$$

and

$$-\frac{dV}{dt} = V \sin \theta_E \frac{dV}{dY} \quad (15)$$

Substituting and using the approximate conductivity, Eq. (6) becomes

$$\frac{d \left( \frac{V}{V_E} \right)}{\left( \frac{V}{V_E} \right)^{1 + 2/5(N-1)}} = \frac{C_D \pi}{2 \sin \theta_E} \left( \frac{\rho_0}{m_B} \right) \left( \frac{\sigma_0 m^2 \epsilon}{\rho_0 V_E 4\pi^2} \right)^{2/5} e^{-.6\beta Y} dY \quad (16)$$

Integrating Eq. (16) and using the boundary condition that at  $y = y_E$ ,  $V = V_E$ , the velocity history is

$$\frac{V}{V_E} = \left( 1 - \alpha \left( e^{-.6\beta Y_E} - e^{-.6\beta Y} \right) \right)^{1/\beta} \quad (17)$$

where

$$\alpha = 2/5(N-1) \frac{\pi C_D \epsilon^{2/5}}{1.2 \sin \theta_E} \left( \frac{\rho_0}{m_B \beta^3} \right) \left( \frac{\sigma_0 m^2 \beta^5}{\rho_0 V_E 4\pi^2} \right)^{2/5} \quad (18)$$

$$\beta = \frac{1}{-2/5(N-1)} \quad (19)$$

The deceleration is

$$-\frac{dV}{dt} = V_E^2 \sin \theta_E \left( \frac{V}{V_E} \right) \frac{d \left( \frac{V}{V_E} \right)}{dY} \quad (20)$$

$$-\frac{dV}{dt} = -.6 V_E^2 \sin \theta_E \beta \gamma^\alpha e^{-.6\beta\gamma} \left[ 1 - \alpha \left( e^{-.6\beta\gamma_E} - e^{-.6\beta\gamma} \right) \right]^{2\gamma-1} \quad (21)$$

The altitude of maximum deceleration is obtained by setting the derivative of the deceleration with respect to altitude equal to zero,

$$\frac{d}{d\gamma} \left( -\frac{dV}{dt} \right) = 0 \quad (22)$$

and the altitude of peak deceleration is then

$$\gamma_{MAX.G} = \frac{1}{.6\beta} \ln \left( \frac{1}{2\gamma} \left[ -\frac{1}{\alpha} + e^{-.6\beta\gamma_E} \right] \right)^{-1} \quad (23)$$

For initial re-entry altitudes at or above 100 km, the term

$$e^{-.6\beta\gamma_E} \approx 0 \quad (24)$$

Thus the altitude of maximum deceleration becomes

$$\gamma_{MAX.G} = \frac{1}{.6\beta} \ln \left( -\frac{1}{2\gamma\alpha} \right)^{-1} \quad (25)$$

If Eq. (25) is substituted into Eq. (17), the velocity at peak g's is given by

$$\left( \frac{V}{V_E} \right)_{MAX.G} = \left[ 1 - \frac{1}{2\gamma} \right]^\alpha \quad (26)$$

which for the slope of the log of electrical conductivity curve of Fig. 1, i.e.,  $N = 5.14$ , gives

$$\left( \frac{V}{V_E} \right)_{MAX.G} = .695 \quad (27)$$

The vehicle deceleration at this point is

$$\left( -\frac{dV}{dt} \right)_{MAX.G} = \left[ \frac{\beta V_E^2 \sin \theta_E}{2e} \right] \left[ \left\{ 6e \left( 1 + \frac{1}{5}(N-1) \right) \right\}^{-5(N-1)-1} \right] \quad (28)$$

The above can be re-arranged such that the first term in brackets is the peak deceleration of a purely aerodynamic vehicle while the second term represents the modification of the deceleration arising from the MHD forces. Again, for  $N = 5.14$

$$\left( -\frac{dV}{dt} \right)_{MAX.G} = \left[ \frac{\beta V_E^2 \sin \theta_E}{2e} \right] (.43) \quad (29)$$

Thus the peak deceleration for an MHD vehicle varies with scale height, re-entry velocity and re-entry angle identically as a purely aerodynamic vehicle<sup>6</sup>, but reduced by 57%. This reduction is due to the effective drag modulation caused by the MHD shock radius change with density. The reduction term arising from the MHD interaction has been evaluated for various values of the conductivity law. The reduction in peak g's is not sensitive to the velocity dependence of the electrical conductivity. The reduction in peak deceleration varies slowly with N, with increasing values of N causing increasing reductions in the peak deceleration.

## B. Re-Entry at High Magnetic Reynolds Number

For high magnetic Reynolds numbers the radius of the shock is determined by the condition that the magnetic pressure is in balance with the dynamic pressure ( $\rho v^2$ ).<sup>4</sup>

$$\frac{B^2}{2\mu_0} = \rho V^2 \quad (30)$$

Again the assumption was made that the magnetic field strength is given by the far field of a single loop of wire

$$B = \frac{m}{2\pi R^3} \quad (31)$$

The radius of the shock is then

$$R = \left( \frac{m^2}{8\pi^2\mu_0\rho V^2} \right)^{1/6} \quad (32)$$

and the area of the shock is

$$A = \pi R^2 = \pi \left( \frac{m^2}{8\pi^2\mu_0\rho V^2} \right)^{1/3} \quad (33)$$

Again assuming a straight line trajectory, the following differential equation arises from Eq. (6):

$$\frac{d\left(\frac{V}{V_E}\right)}{\left(\frac{V}{V_E}\right)^{1/3}} = \frac{C_D \pi}{2 m_B} \left( \frac{m^2}{8\pi^2\mu_0} \right)^{1/3} \left( \frac{S_0}{V_E} \right)^{2/3} \frac{1}{\sin\theta_E} e^{-2/3\beta y} dy \quad (34)$$

If Eq. (34) is integrated with the boundary condition that  $V = V_E$  at  $y = y_E$ , the velocity history is

$$\frac{V}{V_E} = \left( 1 + \alpha_1 \left( e^{-2/3\beta y_E} - e^{-2/3\beta y} \right) \right)^{3/4} \quad (35)$$

where

$$\gamma_1 = 3/2 \quad (36)$$

and

$$\alpha_1 = \frac{C_D \pi}{2 m_B \sin \theta_E} \left( \frac{m^2}{8 \pi^2 \mu_0} \right)^{1/3} \left( \frac{S_0}{V_E} \right)^{2/3} \frac{1}{\beta} \quad (37)$$

The deceleration history is obtained as before

$$-\frac{dV}{dt} = V_E^2 \sin \theta_E \left( \frac{V}{V_E} \right) \frac{d \left( \frac{V}{V_E} \right)}{d\gamma} \quad (38)$$

$$-\frac{dV}{dt} = 2/3 V_E^2 \sin \theta_E \beta \gamma_1 \alpha_1 e^{-2/3 \beta \gamma} \left( 1 + \alpha_1 \left( e^{-2/3 \beta \gamma_E} - e^{-2/3 \beta \gamma} \right) \right)^{2 \gamma_1 - 1} \quad (39)$$

From

$$\frac{d}{d\gamma} \left( -\frac{dV}{dt} \right) = 0 \quad (40)$$

the altitude of peak deceleration is

$$\gamma_{MAX.G} = \frac{3}{2\beta} \ln \left( \frac{1}{2 \gamma_1 \alpha_1} \left( 1 + \alpha_1 e^{-2/3 \beta \gamma_E} \right) \right)^{-1} \quad (41)$$

For initial re-entry altitudes of about 100 km the term  $e^{-2/3 \beta \gamma_E}$  is negligible so that the altitude of peak deceleration becomes

$$\gamma_{MAX.G} = \frac{3}{2\beta} \ln ( 2 \gamma_1 \alpha_1 ) \quad (42)$$

The velocity at peak g's is

$$\left(\frac{V}{V_E}\right)_{MAX.G.} = \left(1 - \frac{1}{2\mu_1}\right)^{\mu_1} = \left(\frac{2}{3}\right)^{3/2} = .55 \quad (43)$$

and the deceleration at peak g's is

$$\left(-\frac{dV}{dt}\right)_{MAX.G.} = \frac{\beta V_E^2 \sin \theta_E}{2e} \left(\frac{2e}{3} \left[1 - \frac{1}{2\mu_1}\right]^{2\mu_1-1}\right) \quad (44)$$

For

$$\mu_1 = 3/2$$

$$\left(-\frac{dV}{dt}\right)_{MAX.G.} = \left[\frac{\beta V_E^2 \sin \theta_E}{2e}\right] (.80) \quad (45)$$

The maximum deceleration encountered is then reduced by only twenty per cent due to MHD forces for the high Magnetic Reynolds number case, due to the smaller area change compared to the previous case.



## SECTION III

### VERTICAL RE-ENTRY

#### A. Dynamics

##### Analytical Results

The simplified analyses have been applied to the case of MHD re-entry vehicle entering the atmosphere vertically at velocities of 40,000 and 50,000 feet per second, typical of the return of a probe from Mars or Venus. The solution of vertical re-entry at these speeds requires the use of high  $R_M$  theory, for the early part of the re-entry followed by low  $R_M$  theory when both predict the same shock radii. A typical re-entry history, calculated using a combination of the two analyses is shown in Figs. 2 and 3, for a re-entry velocity of 40,000 feet per second, a weight of 1000 pounds and a magnetic moment of 10 weber-meters. Transition from high to low  $R_M$  theory occurs at 96,000 feet. A maximum deceleration of 328 g's is experienced at this altitude. The fact that the radius of curvature predicted on the basis of low  $R_M$  theory decreases more rapidly with altitude than that predicted on the basis of high  $R_M$  theory causes the deceleration to decrease sharply from the level reached at the altitude where the radii of curvature are equal. In a more detailed calculation the flow would change from the one characterization to the other gradually. This would lower the maximum deceleration encountered and raise the altitude of peak deceleration above that predicted on the basis of instantaneous change from one flow model to the other. In the low  $R_M$  theory, it is assumed that the density ratio across the shock is constant. The low  $R_M$  portion of the trajectory (Figs. 2 and 3) was calculated using the magnitude of  $\epsilon$  at transition from high to low  $R_M$  theory (i. e.,  $\epsilon = .078$ ). With the exception of magnetic Reynolds number, no significant differences in the trajectory parameters were noted when the solution was recalculated assuming  $\epsilon$  constant at .064. The magnetic Reynolds number used in these calculations was based on a length of  $\epsilon R$  and has a magnitude greater than unity for altitudes above 100,000 feet. The maximum deceleration is 320 g's, only slightly less than the 336 g's predicted on the basis of only high  $R_M$  re-entry theory; still 21% less than the deceleration of a purely aerodynamic vehicle. The radius of the MHD supported shock decreases from 4.1 meters at 300,000 feet to 1.0 meters at 100,000 feet. The magnetic field strength at the shock is shown in Fig. 3; it increases with decreasing altitude due to the diminishing radius of the shock. The magnitude of the magnetic field strength at the shock wave is 1500 gauss at peak deceleration. The magnitude of the Hall coefficient  $\omega\tau$  is also shown in Fig. 3 and is less than unity from re-entry to 80,000 feet.

The mass of the coil was related to its magnetic moment. This is defined as:

$$m = \mu_0 I A = \mu_0 I \pi b^2 \quad (46)$$

where  $\mu_0$  is the permeability of free space,  $I$  is the current in amps flowing in a single loop of wire.  $A$  is the projected area of the loop of wire, square meters and  $b$  is the radius of the coil in meters.

Now

$$I = i A_1 \quad (47)$$

where  $i$  is the current density in the wire and  $A_1$  is the cross-sectional area of the wire.

From Eqs. (46) and (47)

$$A_1 = \frac{m}{\mu_0 i A} = \frac{m}{\mu_0 i \pi b^2} \quad (48)$$

The mass of the conductor is the volume of the conductor, (i. e., cross-sectional area times circumference) multiplied by the density of superconducting material  $\rho_c$

$$m_c = \frac{2 m}{\mu_0 i b} \rho_c$$

The mass of the coil is shown in Fig. 3 for a current density of  $10^5$  amps/square centimeter,<sup>7,8</sup> a mass density of  $8.4 \times 10^3$  kilograms per cubic meter and a coil radius equal to the MHD shock radius at each altitude. The variation of the altitude and deceleration at the point where high and low magnetic Reynolds number theories predict equal shock radii is shown in Figs. 4 and 5 for variations in the magnitude of the magnetic moment, for re-entry velocities of 40,000 and 50,000 feet per second, respectively. The altitude and the magnitude of peak deceleration predicted by the pure high  $R_M$  theory is also shown in Fig. 4 for comparison. As the magnetic moment is decreased, the altitude at which equivalent shock radii occur becomes increasingly higher than that predicted by the pure high  $R_M$  theory. The peak deceleration increases substantially below the peak deceleration predicted by the pure high  $R_M$  theory as the magnetic moment is reduced.

### Computer Results

The accuracy of the analytical results has been checked by numerical computer calculations. Trajectory equations<sup>9</sup> are incorporated which describe the two degrees of freedom motions of a body over a curved earth. The gas flow parameters required in the calculations, such as electrical conductivity, density ratio across the shock are calculated assuming a normal shock wave and equilibrium thermodynamics. The shock radii and trajectories predicted by the high  $R_M$  analytical results and high  $R_M$  machine

calculations agree. However, the magnetic Reynolds number from the machine calculation is well below that predicted by the analytical result at high altitudes. The difference is due to the fact that a constant density ratio of .078 was used in the analytical results whereas  $\epsilon$  in the machine calculations varies but is .049 at 300,000 feet. The Hall coefficient  $\omega\tau$  and magnetic field strength predicted by both methods agree. A comparison of machine calculations with the predictions of the low  $R_M$  theory was also made and agreement between the methods was again noted.

A numerical results for the equivalent re-entry of Figs. 2 and 3 are shown in Figs. 6 and 7. In this case, the two radii become equal at 110,000 feet and the peak deceleration is 278 g's at this point. The deceleration level determined by the machine calculations is below that predicted by the analytical results because the 1959 ARDC atmosphere model used has a larger scale height in the altitude regime near peak deceleration. The analytical results assumed an exponential atmosphere. The deceleration experienced by the MHD vehicle is 37% lower than the 440 g's deceleration of an aerodynamic vehicle entering with the same initial conditions.

The agreement between the computer and analytical results indicates that the latter method may be used with confidence to obtain trajectory data over a variety of re-entry conditions.

The concept for a re-entry vehicle employing MHD forces to diminish deceleration loads used here consists of an aerodynamic body in which a coil is placed. The coil size (i. e., the body size) should be somewhat smaller than the radius of the MHD supported shock at peak deceleration. This will allow the vehicle to reach the altitude of peak deceleration before the aerodynamic body is exposed, thus, ensuring that no deceleration greater than that predicted on the basis of the MHD interaction is reached. The net decrease in overall re-entry systems weight arising from this reduction in maximum deceleration was not examined since it must be answered by engineering calculations for a specific design. All results discussed have been for the case of constant magnetic moment during re-entry. Even lower maximum deceleration can be achieved by varying the magnetic moment (i. e., current in the magnetic coil) during re-entry to further increase the variation of the radius of the shock.

## B. Heating

A comparison of the heat load experienced during vertical re-entry by a vehicle employing MHD interaction and a blunt aerodynamic vehicle was made. The physical size of the MHD vehicle was chosen equal to the radius of the MHD shock at peak deceleration. This choice will essentially assure that the diminution of the maximum deceleration was realized. The size and weight of the comparison aerodynamic vehicle was the same as the MHD vehicle. The radius of curvature of the heat shield of the aerodynamic vehicle was equal to the diameter of the vehicle, which is a bluntness similar to that of the Mercury spacecraft.

The energy flux from a gas to body depends on the condition of the radiating gas and the geometry. The radiating gas volume depends on the nature of the flow. For the case of low magnetic Reynolds number, our description of the interaction between a hypersonic flow and a three-dimensional magnetic dipole follows Ref. 5. The general features of such a flow are shown in Fig. 8. A strong shock is formed ahead of the dipole. Behind the shock there is a thin deceleration layer which is a region in which the velocity component parallel to the shock is larger than the component normal to the shock. There is in addition, a slow flow region behind the deceleration layer where the Mach number is very low. A particularly important feature of Fig. 8 is the existence of a limiting field line which is a streamline, which the flow does not penetrate. Therefore no flow is in contact with the body surface and the single heating mechanism for a re-entry vehicle employing this MHD interaction is radiative heating. The radiating gas volume is the volume between the shock front and the limiting field line. The shape of the magnetic field lines of a circular loop of current carrying wire is shown in Fig. 9.<sup>12</sup> For low magnetic Reynolds number flow, the field lines are not effected by the interaction. The magnetic field lines are slightly oblate figures, being flattened in the direction of the vertical axis. The relationship between the inner and outer location of the magnetic field lines are shown for  $\beta_1 = 90^\circ$  in Fig. 10.  $R_I/b$  is the inner location of a particular field line normalized with respect to the radius  $b$  of the current carrying loop, while  $R_O/b$  is the outer location of the same field line. For purposes of radiation calculations, it is assumed that the limiting field line is that magnetic field line which is tangent to the shock front at  $\beta_1 = 90^\circ$ , and in addition that the shape of the limiting field line can be approximated by a circle of radius

$$R_I = \frac{R_O - R_I}{2}$$

centered at

$$l = R_I + \frac{R_O - R_I}{2}$$

It is also assumed that the gas volume between the hemispherical shock wave and the toroid of semi-circular cross-section is filled with isothermal gas with the temperature and density it would have behind a normal shock.

At high magnetic Reynolds number, the interaction between a hypersonic flow and a magnetic dipole has been treated by Levy,<sup>4</sup> Hurley,<sup>13</sup> Dungey,<sup>14</sup> and Zhigulev and Romishevski<sup>15</sup>. The general features of the flow are shown in Fig. 11. A shock wave forms in the gas upstream of the dipole. There is a thin shock layer behind the shock wave. At the back of the shock layer there is a current sheet behind which there is a magnetic field but no plasma. There is a small region of trapped flow at the intersection of the axis of the dipole and the shock wave. Again convective heating is eliminated since the hot gas does not penetrate into the region of the dipole. The radiating gas volume for high  $R_M$  interaction is approximated

by a hemispherical shell thickness  $\epsilon R$ , where  $\epsilon$  is the density ratio across the shock wave. The shock layer is assumed to be filled with isothermal gas with gas conditions representative of those behind a normal shock.

For a spherical coordinate system with its origin at dA, and the solid angle  $d\omega$  expressed in terms of the angles  $\beta_1$  and  $\phi$ , the hemispherical emissivity can be written as (Appendix A)

$$\bar{\epsilon} = \frac{1}{\pi} \int_{\phi=0}^{\phi=2\pi} \int_{\beta_1=0}^{\beta_1=\pi/2} \left( 1 - e^{-\frac{(\bar{\epsilon}/L) S}{2}} \right) \sin \beta_1 \cos \beta_1 d\beta_1 d\phi$$

where  $(\bar{\epsilon}/L)$  is the emissivity per unit length and  $S$  is the distance in the absorbing gas and may be a function of  $\beta_1$  and  $\phi$ . This equation may be integrated for a specific shape of the radiating gas volume.

The determination of the emissivity of the low magnetic Reynolds number gas volume including self-absorption, is discussed in Appendix A. The emissivity of the low  $R_M$  MHD gas volume for an optically thin gas is shown in Fig. 12 normalized with respect to the emissivity per unit length  $(\bar{\epsilon}/L)$  and the radius of the shock,  $R$ , i.e.,  $\bar{\epsilon}/(\bar{\epsilon}/L)R$ . For large shock to coil radius ratios, the radiating gas volume decreases due to the increasing size of the toroidal volume from which the radiating gas is excluded. This results in a reduction of the radiant heat transfer by forty percent at a radius ratio of 5.

The ratio  $\bar{\epsilon}_* / (\bar{\epsilon}/L)R$  is also shown for an optically thin hemispherical gas volume radiating to the center of its base of (Appendix A). The emissivity of a cylindrical approximation to the low  $R_M$  radiation volume is also shown for comparison. The cylinder radius is assumed equal to the inside radius  $R_I$  of the limiting field line, while the cylinder length is equal to the outside radius  $R_O$  of the same field line. It is noted that the cylindrical approximation, although mathematically tractable for optically thin gas (Appendix B), is not a sufficiently accurate means of estimation.

The emissivity for the hemispherical shell, i.e., the radiating volume for the high magnetic Reynolds number case is constant (Appendix C) and approximately

$$\frac{\bar{\epsilon}}{(\bar{\epsilon}/L)R} = \frac{\epsilon}{2} \approx \frac{1}{20}$$

It can be seen that the radiation heat transfer in the high  $R_M$  region can be a factor of ten less than that in the low  $R_M$  region for small shock to coil radius ratios. It is still a factor of 6 less for a shock to coil radius ratios of five. As for aerodynamic vehicles, the peak radiative heating for MHD vehicles occurs at an altitude above the altitude of peak deceleration whether the gas is optically thick or thin and thus the radiant heat transfer is determined by the emissivity of the high  $R_M$  hemispherical shell gas volume.

If it is assumed that the trajectory is given by the high magnetic Reynolds number theory, that the gas is optically thin, that the density of the atmosphere varies exponentially and that the density ratio  $\epsilon$  across the shock is constant, the radiative heat transfer is related to the emissivity per unit length, the temperature of the gas and the radius of the shock

$$\dot{q}_{RAD} \propto \left( \frac{\bar{\epsilon}}{L} \right) T^4 R$$

Then the radiative heat transfer is a function of altitude alone. From Kivel and Bailey,<sup>16</sup>  $(\bar{\epsilon}/L)$  in the temperature range  $T = 12000^\circ\text{K}$  and the density region of  $\log(\rho/\rho_0) = -1$ , is

$$\frac{\bar{\epsilon}}{L} \propto \rho^{1.2} T^{6.8}$$

For velocities near 40,000 feet per second and altitudes from 400,000 to 100,000 feet, the temperature can be approximated by

$$T \propto \rho^{0.5} V^{1.2}$$

and  $R$  is

$$R \propto \rho^{-1/6} V^{-1/3}$$

Therefore

$$\left( \dot{q}_{RAD} \right)_{M.H.D} \propto \rho^{1.47} V^{11.6}$$

but

$$\rho = \rho_0 e^{-\beta y}$$

and

$$V = V_E \left( 1 - \alpha_1 e^{-2/3 \beta y} \right)^{\gamma_1}$$

where

$$\gamma_1 = 3/2$$

The altitude of maximum radiation heating can be found by substituting the expressions for density and velocity into the radiant heat transfer equation. The altitude of maximum radiative heating, assuming an optically thin gas is

$$y_{MAX} \dot{q}_{RAD} = \frac{3}{2\beta} \ln(8.9\alpha_1)$$

For the case of an optically thick gas, the radiant heating is proportional to the temperature to the fourth power.

$$\dot{q}_{RAD} \propto T^4$$

As shown before

$$T \propto \rho^{.05} V^{1.1}$$

$$\therefore \dot{q}_{RAD} \propto \rho^{.20} V^{4.4}$$

Again

$$\rho = \rho_0 e^{-\beta \gamma}$$

$$V = V_E (1 - \alpha_1 e^{-2/3 \beta \gamma})^{1/2}$$

The altitude of maximum radiative heating, for an optically thick gas

$$\gamma_{MAX} \dot{q}_{RAD} = \frac{3}{2\beta} \ln(23\alpha_1)$$

Previously the altitude of peak deceleration high  $R_M$  re-entry was determined as

$$\gamma_{MAX C} = \frac{3}{2\beta} \ln(3\alpha_1)$$

Therefore, the maximum radiative heat transfer occurs at an altitude above the altitude of peak deceleration in a high  $R_M$  region with radiative heat transfer governed by the emissivity of the hemispherical shell gas volume.

The stagnation point radiative heat load,  $\int \dot{q}_{RAD} dt$ , experienced during re-entry by MHD vehicles and a comparison with aerodynamic vehicles is shown in Figs. 13 and 14 for re-entry velocities of 40,000 and 50,000 feet per second respectively. The emissivity ratio  $\bar{\epsilon}/(\frac{\bar{\epsilon}}{L})R$  for the aerodynamic vehicle, assuming optically thin gas, is .18 (Appendix D).

Since the radius of the MHD supported shock is approximately equal to the radius of the aerodynamic body at peak heating (they are exactly equal at peak deceleration), an estimate of the ratio of the total radiative heat load experienced by the aerodynamic vehicle to that by the MHD vehicle should be in the ratio of the emissivities

$$\frac{\left( \frac{\bar{\epsilon}}{(\frac{\bar{\epsilon}}{L})R} \right)_{AERODYNAMIC}}{\left( \frac{\bar{\epsilon}}{(\frac{\bar{\epsilon}}{L})R} \right)_{MHD}} = \frac{.18}{.05} = 3.6$$

The optically thin results indicate that radiative heating of the aerodynamic vehicle should be 3.6 times that of the MHD vehicle. The heat load of the aerodynamic vehicle is larger than 3.6 times the MHD heat load (Fig. 13). This additional difference results from the fact that the gas volume of the aerodynamic vehicle is not optically thin and though the MHD and

aerodynamic vehicles have the same  $W/C_D A$  at peak deceleration, the MHD vehicle has a larger drag at higher altitudes which modifies the trajectory resulting in a slightly lower temperature for its radiating gas volume. The aerodynamic vehicle is plotted versus magnetic moment in Fig. 13 in the sense that there exists a particular comparison aerodynamic vehicle for each MHD vehicle (i. e., each magnitude of magnetic moment). The calculation of radiant heat load for both the MHD and aerodynamic vehicles included self-absorption in gas.

Estimates of the weight required to protect the MHD and aerodynamic vehicles from these heat loads are shown in Figs. 15 and 16 for re-entry velocities of 40,000 and 50,000 ft/sec respectively. The total weight for the MHD vehicles includes weight allowance for the superconducting wire, coil structure required to carry the loads arising from the presence of current carrying conductors, dewar and ablation material to dissipate the radiant heat load. The weight for the aerodynamic vehicles is that weight of ablation material required to protect against the heat load. It is assumed that the vehicles receive the stagnation point heat load over their entire face. The total weight for the MHD vehicles are shown for both a current carrying capability of  $10^5$  amps/cm<sup>2</sup> and  $10^6$  amps/cm<sup>2</sup>. The former capability has been demonstrated in a single wire and is close to realization in a coil. The latter capability is futuristic, however, the ultimate limit of superconducting materials is estimated to be  $10^7$  amps/cm<sup>2</sup> so that  $10^6$  amps/cm<sup>2</sup> may be achievable in the future. Stekly<sup>7</sup> indicates that coils will be self-supporting for a current density of  $10^5$  amps/cm<sup>2</sup> if the superconducting material has an allowable stress level greater than 80,000 psi. At a current density of  $10^6$  amps/cm<sup>2</sup>, structure material is required to support the magnetic coil. The structural weight was estimated using the results of Levy<sup>19</sup> for the minimum possible structural weight. Levy showed that a minimum possible structural weight results if all the structure is in tension and that under these conditions the structural mass required is

$$M_s = \frac{\rho_s}{\sigma_w} E$$

where  $\rho_s$  is the density of the structural material,  $\sigma_w$  is the maximum working stress and  $E$  is the total magnetic energy stored. If the strength to weight ratio of the structural material used is equal to that of titanium stressed to 230,000 psi, then a minimum structural weight of  $2.9 \times 10^{-6}$  Kg/joule of stored magnetic energy results.

The maximum energy stored in the coils for the case of re-entry at 40,000 feet per second was  $2.5 \times 10^6$  joules at  $m = 100$  while at  $V = 50,000$  feet/sec the maximum energy is  $3.7 \times 10^6$  joules at  $m = 100$ . The maximum structural mass would be less than 10 kilograms. A density of  $8.4 \times 10^3$  kilograms/M<sup>3</sup> is used for the superconducting material in the present study. The weight of the dewar is the surface area of the dewar times the surface density. The dewar surface area was determined from Ref. 7 and a dewar surface density of 1 lb/ft<sup>2</sup> is used. It should be noted that the dewar surface area of Ref. 7 is for a particular geometry where the radius of the circular cross-section conductor is 1/3 the radius of the coil.

For the aerodynamic vehicle the entire weight is ablation material. An effective heat of ablation for the ablation material was chosen as 20,000 Btu/lb. This is considerably more effective than present day ablation materials. Figure 15 shows that at 40,000 feet per second entry velocity and a current density of  $10^5$  amps/cm<sup>2</sup> ablation heat protection is lighter, while at  $10^6$  amps/cm<sup>2</sup> the protective weight for both MHD and aerodynamic vehicles is equivalent. At 50,000 feet per second (Fig.16) and a current density of  $10^5$  amps/cm<sup>2</sup> MHD and aerodynamic vehicles have equivalent heat protection weights for small sizes while aerodynamic vehicles with ablation protection are lighter for body sizes larger than 3 feet radius. For  $10^6$  amps/cm<sup>2</sup>, heat protection by MHD is lighter by 200 pounds than ablation material for vehicle radii from 1.0 to 7.0 feet. No allowance has been made in the weight estimates for the MHD vehicles (Figs. 15 and 16) for the reduction in vehicle weight resulting from the fact that the MHD vehicles experience 35 percent less maximum deceleration than the aerodynamic vehicles. The decrease in vehicle weight arising from the decrease in maximum deceleration may be substantial but must be answered by engineering calculations for a specific design.



## SECTION IV

### LIFTING RE-ENTRY

Comparison of MHD and aerodynamic lifting vehicles was made for an entry velocity of 40,000 feet per second and for lift to drag ratios from 1/2 to 4. The use of MHD forces to broaden the re-entry corridor and decrease heat transfer was considered. In this analysis, the MHD vehicle has both L/D and a large blunt shock wave. Physical achievement of this combination has not been realized conceptually and is not considered further. The allowable entry angles for MHD and aerodynamic vehicles along the undershoot and overshoot boundaries are shown in Fig. 17. On the undershoot boundary the vehicle is considered to fly at a positive L/D from entry to pullout with L/D adjustment after pullout to maintain constant altitude until lift can no longer be generated to maintain that altitude. A maximum total deceleration of 12 g's was considered on the undershoot boundary as typical of manned vehicles. The overshoot boundary shown in Fig. 17 was that of Ref. 20. The vehicle is considered to fly a positive L/D trajectory from entry to pullout. At this point negative lift is applied to maintain constant altitude flight. The overshoot boundary is that re-entry angle at which the maximum negative lift capability of the vehicle is required to keep the vehicle from leaving the atmosphere.

The physical radius of the MHD vehicle was chosen to be the radius of the MHD supported shock at peak deceleration on the undershoot boundary. The aerodynamic comparison vehicles were again chosen with the same size and weight at the MHD vehicles. Therefore the MHD vehicle at maximum deceleration on the undershoot boundary has the same  $W/C_D A$  as its comparison aerodynamic vehicle. The MHD vehicle undershoot and overshoot boundaries are shown in Fig. 17 for a vehicle weight of 10,000 pounds and a size which results in a  $W/C_D A$  of 26.6 at peak deceleration (and for the aerodynamic comparison vehicles). The magnetic moment required to produce this  $W/C_D A$  varies with the magnitude of lift to drag ratio; at  $L/D = 1/2$ ,  $m = 86$ ,  $L/D = 1.0$   $m = 72$  and at  $L/D = 4.0$ ,  $m = 32$ .

The allowable entry angles for MHD and aerodynamic vehicles on the undershoot boundary are slightly different. The difference is due to the fact that the MHD vehicles has a larger drag area from entry to pullout which results in an effective  $W/C_D A$  of the MHD vehicle approximately 20 percent lower than that based on peak deceleration conditions. On the overshoot boundary, the MHD vehicles have substantially lower allowable re-entry angles than the aerodynamic vehicles. The MHD vehicle, though still of the same physical size and with the same magnetic moment as on the undershoot boundary now has a much larger drag area over the region from entry to pullout which produces an effective  $W/C_D A$  three (AT  $L/D = 1/2$ ) to five

(L/D = 4.0) times lower than that of the aerodynamic vehicle. These boundaries were determined from numerical calculations utilizing two degree of freedom equations of motion.<sup>9</sup> If Chapman's<sup>21</sup> definition of the overshoot boundary were used, the allowable re-entry angles for the MHD vehicles would be still further reduced from the values shown in Fig. 17.

For re-entry both along the overshoot and undershoot boundaries, the MHD vehicle operates in a region of high magnetic Reynolds number. For lifting re-entries the magnitude of the Hall coefficient,  $\omega\tau$  is a factor that must be considered. The variation of  $\omega\tau$  during a typical re-entry is, at entry (400,000 feet)  $\omega\tau = 4.0$ ,  $\omega\tau$  then decreases from entry to pullout reaching a value of .5 at peak deceleration.  $\omega\tau$  then again increases after pullout. It has been arbitrarily assumed that the MHD interaction with the flow ceases after pullout when the magnitude of  $\omega\tau$  becomes equal to five. This occurs at a velocity of about 29,000 feet per second.

Lift to drag ratios of unity have been produced<sup>22</sup> experimentally in laboratory facilities but to date have not been studied in sufficient detail to design a practical entry vehicle which produces L/D ratios with MHD. It should also be noted that the comparison aerodynamic vehicles were assumed to be large blunt vehicles yet possess high L/D ratios. There are no ways to produce aerodynamic L/D's ratios greater than 1/2 with large blunt objects. High lift to drag ratio aerodynamic bodies are associated with slim, slender, and thin wing body combinations. Thus this study is more comparative than quantitative in that neither of the lifting vehicles represent real configurations.

The re-entry heat load experienced by the lifting MHD and aerodynamic vehicles is shown in Fig. 18. The trajectories followed by MHD vehicles from entry through pull and up to  $\omega\tau = 5$  are such that the MHD interaction is governed high magnetic Reynolds number theory and thus the radiation heating is governed by the hemispherical shell gas model, and the gas is optically thin. The major portion of the re-entry heat pulse is over by the time the Hall coefficient reaches five. The heat load experienced by the MHD vehicle is entirely radiative while the heat load of the aerodynamic vehicle is both convective and radiative. The convective heating is determined by the correlation formula of Kemp and Riddell<sup>23</sup> for the Fay-Riddell theory<sup>24</sup>

$$\dot{q} \sqrt{R_c} = 20800 \sqrt{\rho/\rho_0} \left( \frac{V}{V_c} \right)^{3.25} \left( 1 - \frac{h_{sw}}{h_{s1}} \right) \quad \text{BTU/FT}^2\text{-SEC}$$

where  $\rho$  is mass density,  $U$  is flight velocity,  $U_c$  is circular velocity,  $h_{sw}$  is the stagnation point enthalpy at the body surface,  $h_{s1}$  is the stagnation point enthalpy at the edge of the boundary layer and  $R_c$  is the radius of curvature of the body.

The radiative stagnation point heat load for the MHD vehicle and the radiative and convective stagnation point heat loads for the aerodynamic vehicle are shown in Fig. 18. For the aerodynamic case, the heat load on

the undershoot boundary (convective plus radiative) sizes the amount of ablation material for L/D ratios up to 2.0. For L/D ratios from 2 to 4, the heat load on the overshoot boundary designs the ablation material. On the undershoot boundary, the heat load experienced by the MHD vehicle is one order of magnitude less than the aerodynamic vehicle. On the overshoot boundary, the heat load of the MHD vehicle is two orders of magnitude less.

Estimates of the weight required to protect the MHD and aerodynamic vehicle from these heat loads are shown in Fig. 19. The total weight for the MHD vehicles include weight allowance for superconducting wire, coil structure, dewar and ablation material. The weight shown for the aerodynamic vehicle is entirely ablated material. The effective heat of ablation was again taken as 20,000 Btu/lb. Weights for the MHD vehicles are shown for wire current carrying capability of  $10^5$  amps/cm<sup>2</sup> and  $10^6$  amps/cm<sup>2</sup>. At  $10^5$  amps/cm<sup>2</sup>, the structure is again self-supporting and at  $10^6$  amps/cm<sup>2</sup> the additional structure required is minimal. At a current density of  $10^5$  amps/cm<sup>2</sup>, the MHD vehicle is lighter than the aerodynamic vehicle for all lift to drag ratios. At L/D = 1/2, the MHD heat protection system is 1700 pounds lighter than the aerodynamic vehicle. At L/D = 1/2, the MHD vehicle is 2400 pounds lighter than the aerodynamic vehicle if the current capability is  $10^6$  amps/cm<sup>2</sup>. Thus again, like the vertical re-entry case, the MHD vehicle will show up to considerable advantage as current densities greater than  $10^5$  amps/cm<sup>2</sup> are achieved in superconducting coils.

#### ACKNOWLEDGMENT

The author wishes to express appreciation to Mr. P. H. Rose, Dr. H. E. Petschek and Dr. R. H. Levy for helpful suggestions during the course of this work.

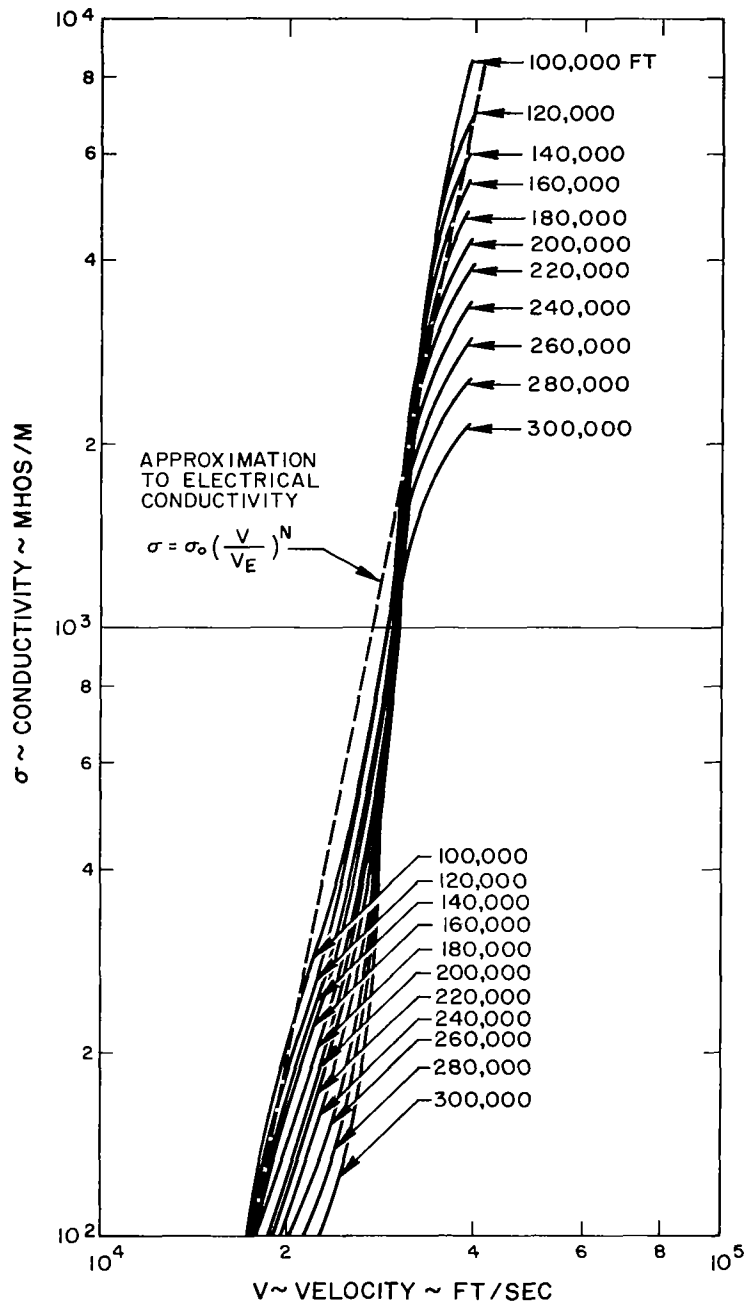


Fig. 1 Approximation to electrical conductivity of equilibrium air.

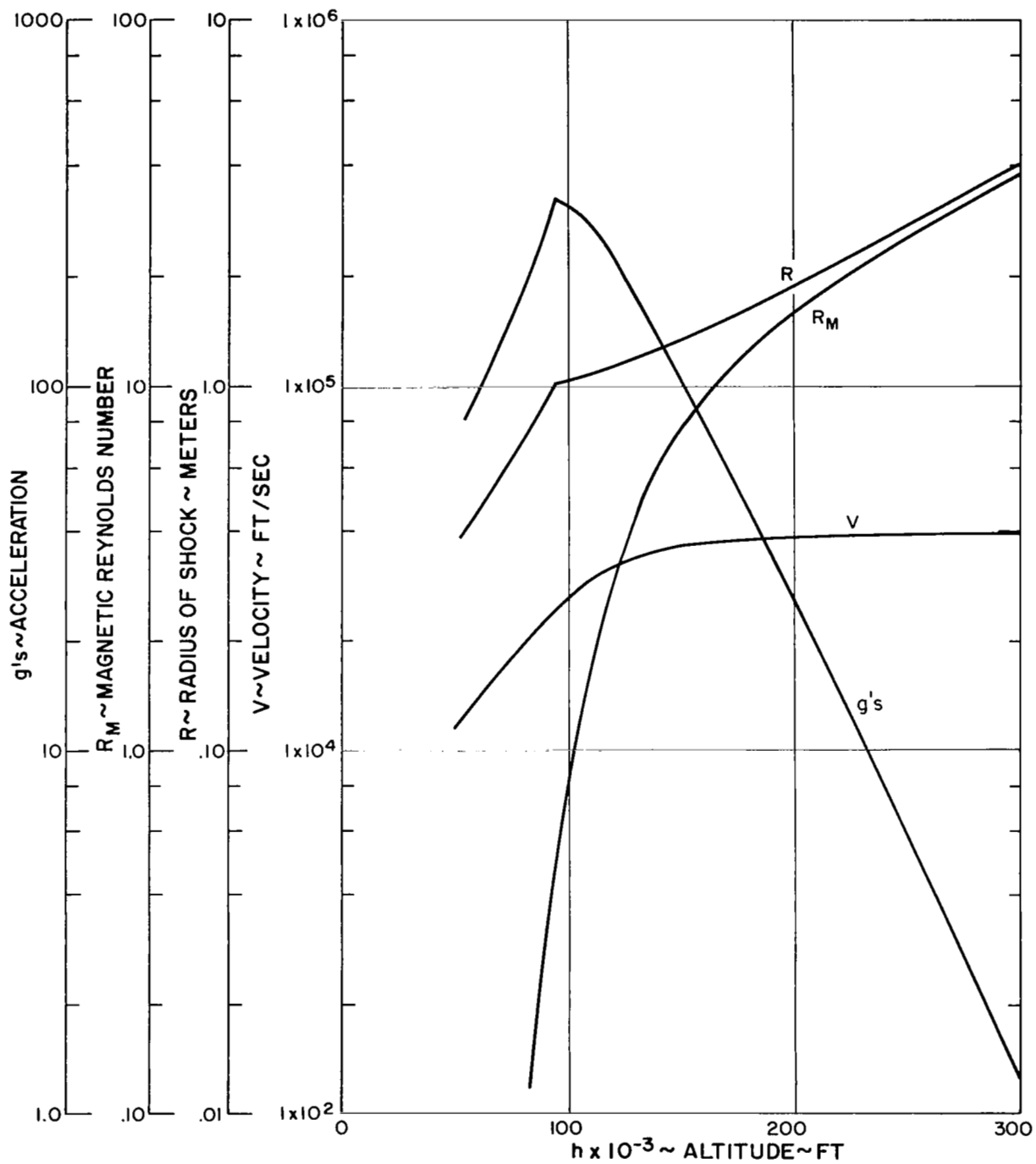


Fig. 2 Re-entry history using combination of high and low magnetic Reynolds number theories.  $R$ ,  $R_M$ ,  $V$ ,  $G'_s$ .

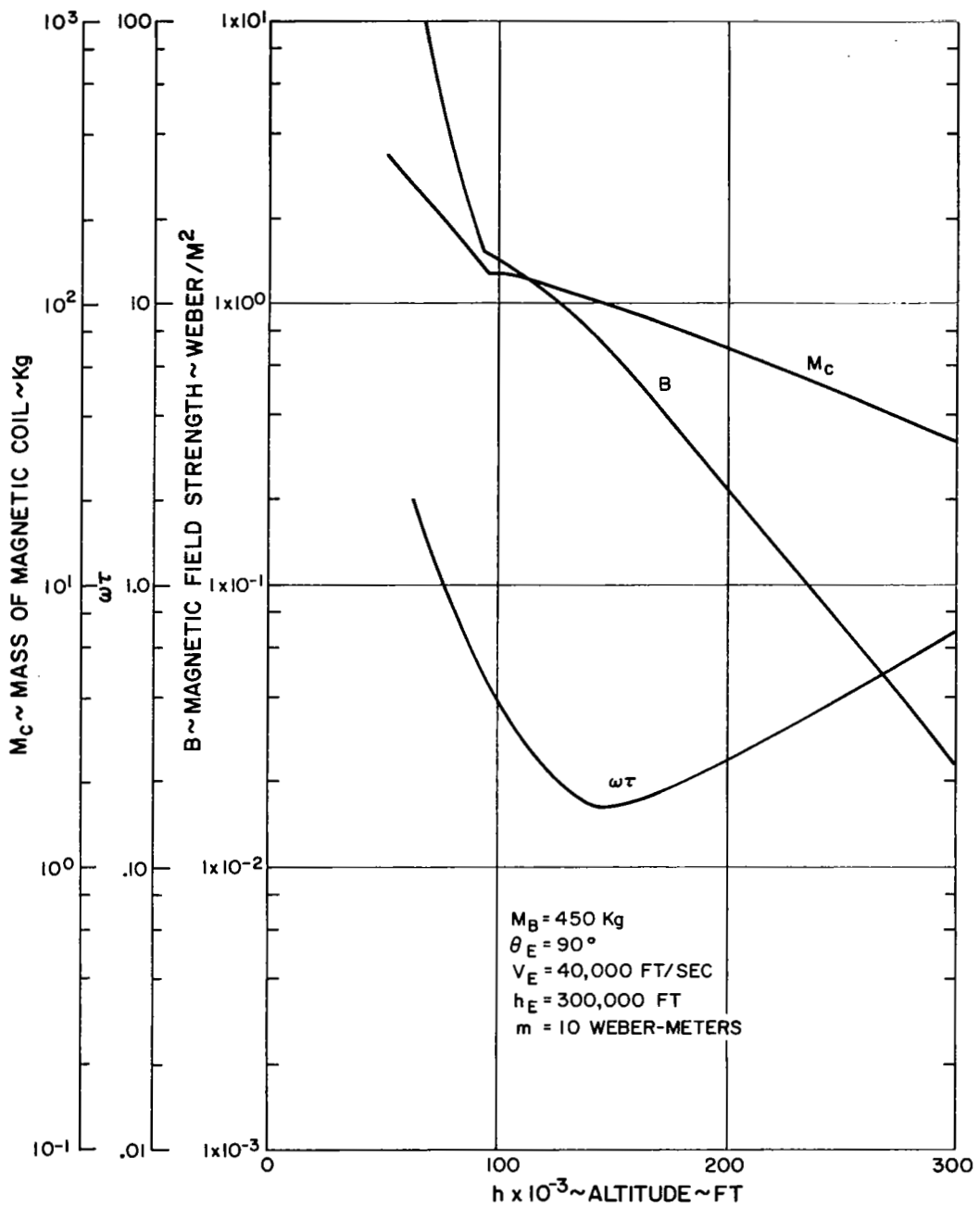


Fig. 3 Re-entry history using combination of high and low magnetic Reynolds number theories.  $B$ ,  $\omega\tau$ ,  $M_C$

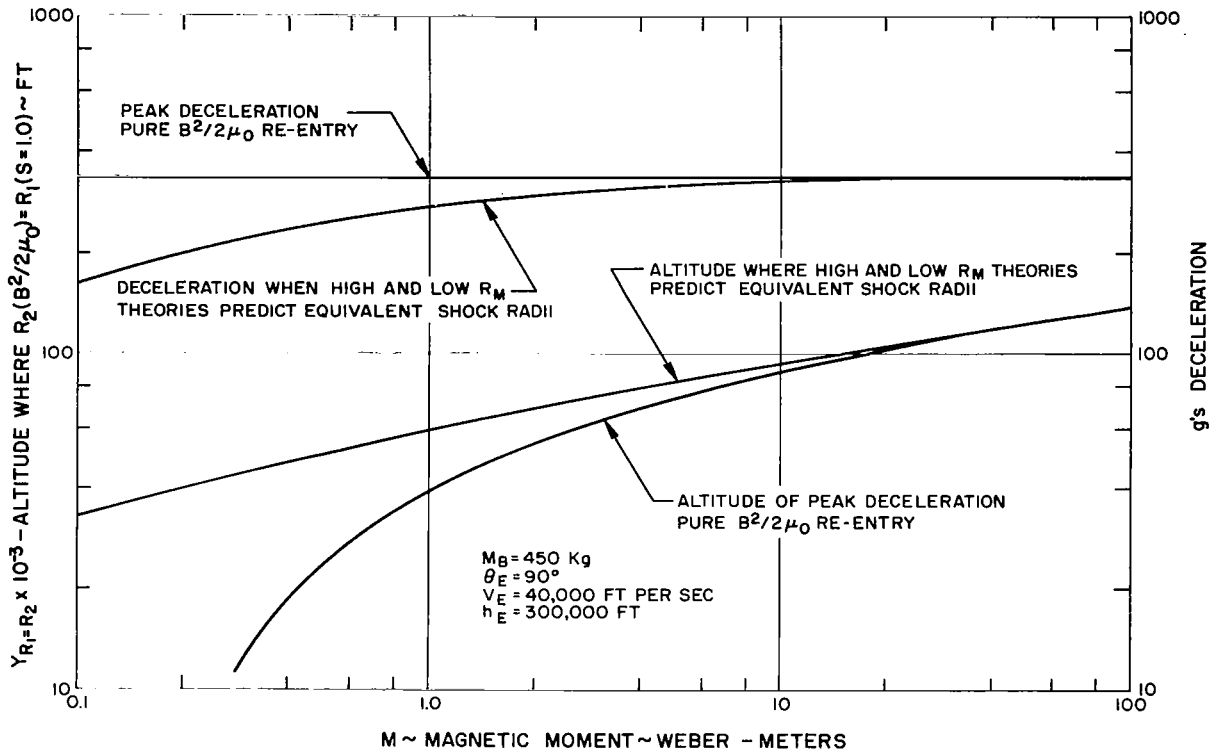


Fig. 4 The altitude and deceleration at transition from high to low  $R_M$  theory  $V_E = 40,000$  ft/sec.

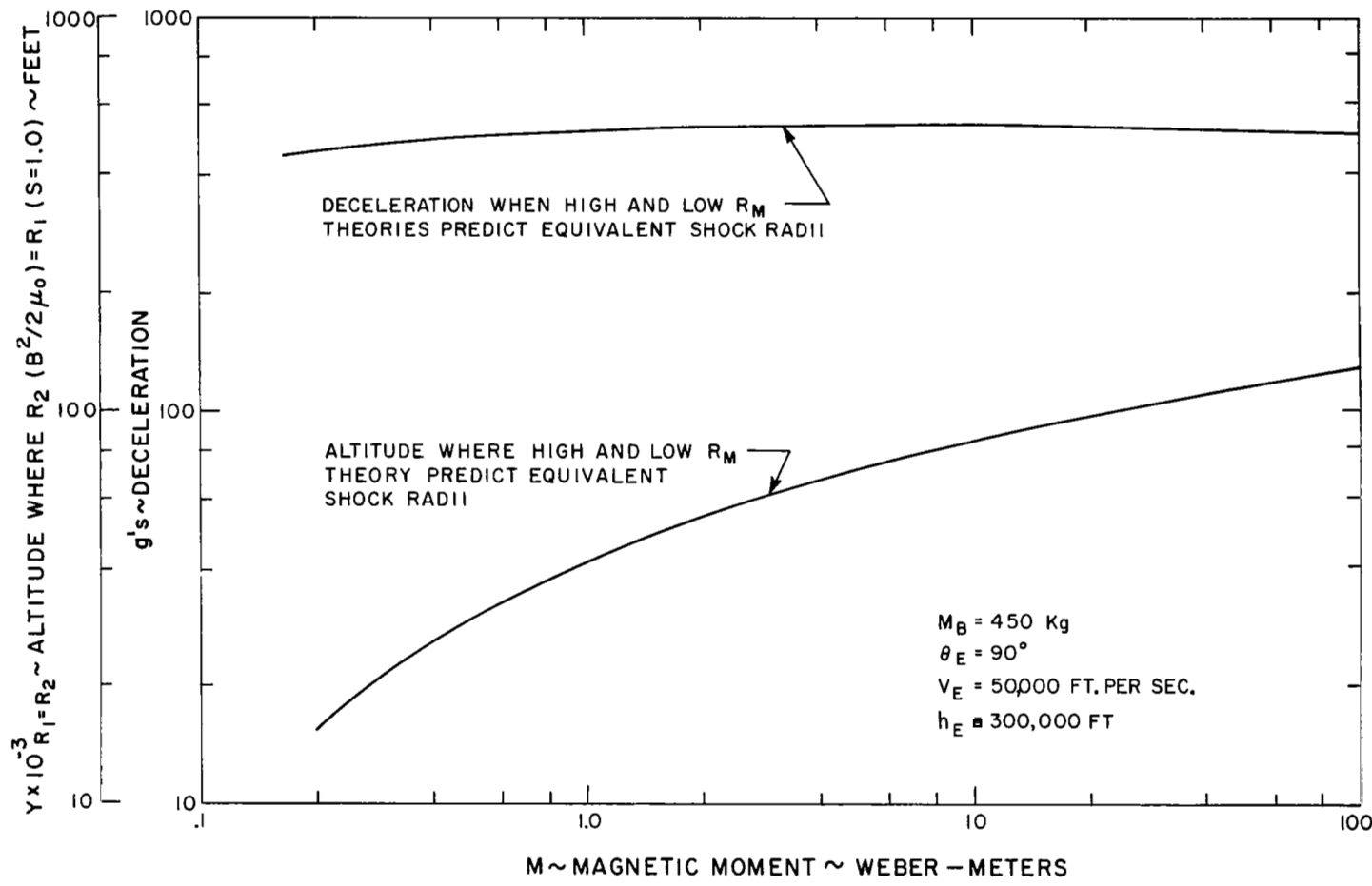


Fig. 5 The altitude and deceleration at transition from high to low R<sub>M</sub> theory V<sub>E</sub> = 50,000 ft/sec.

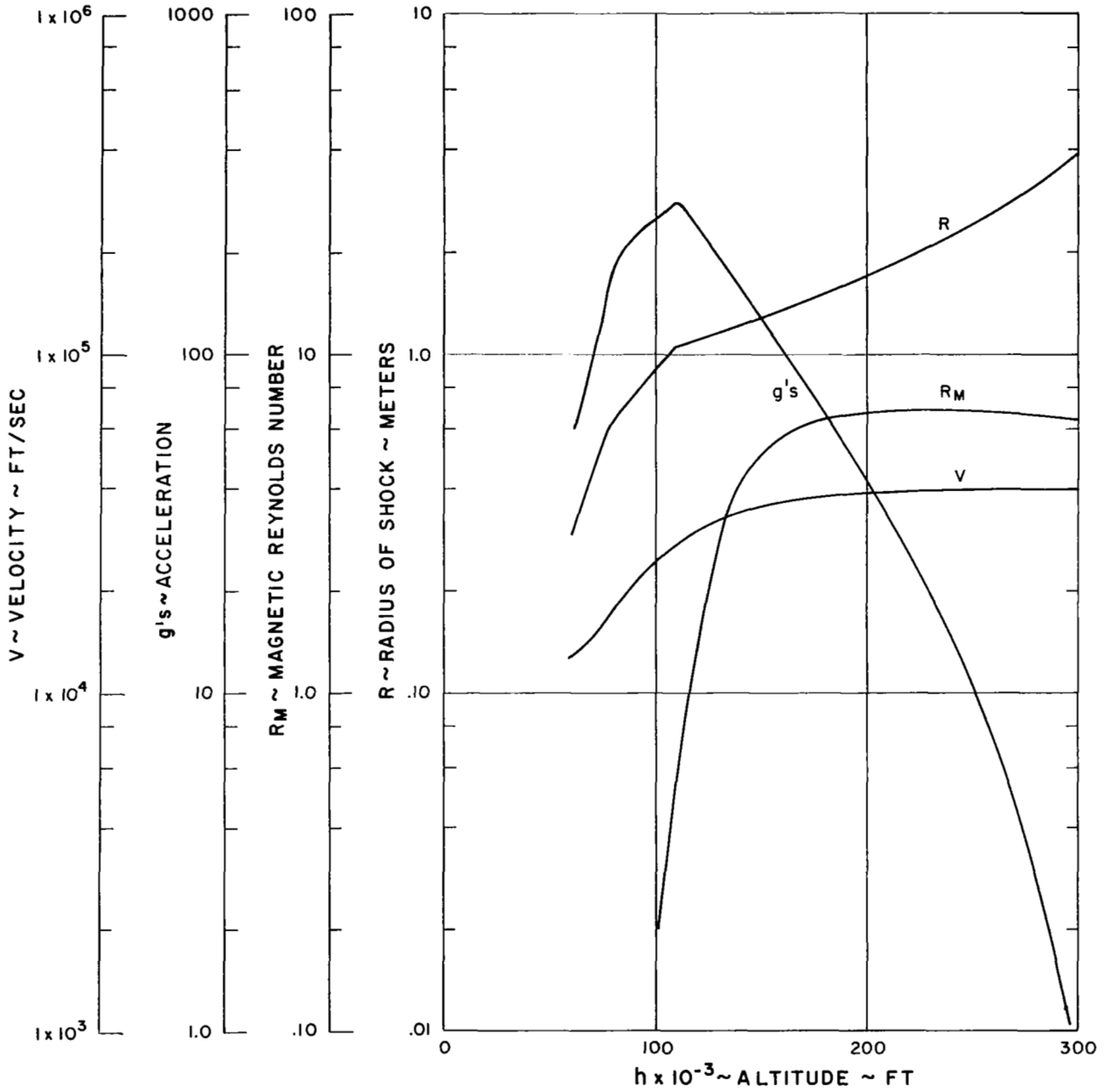


Fig. 6 Computer calculation of re-entry history  $R$ ,  $R_M$ ,  $V$ ,  $G$ 's  
 $V_E = 40,000$  ft/sec.

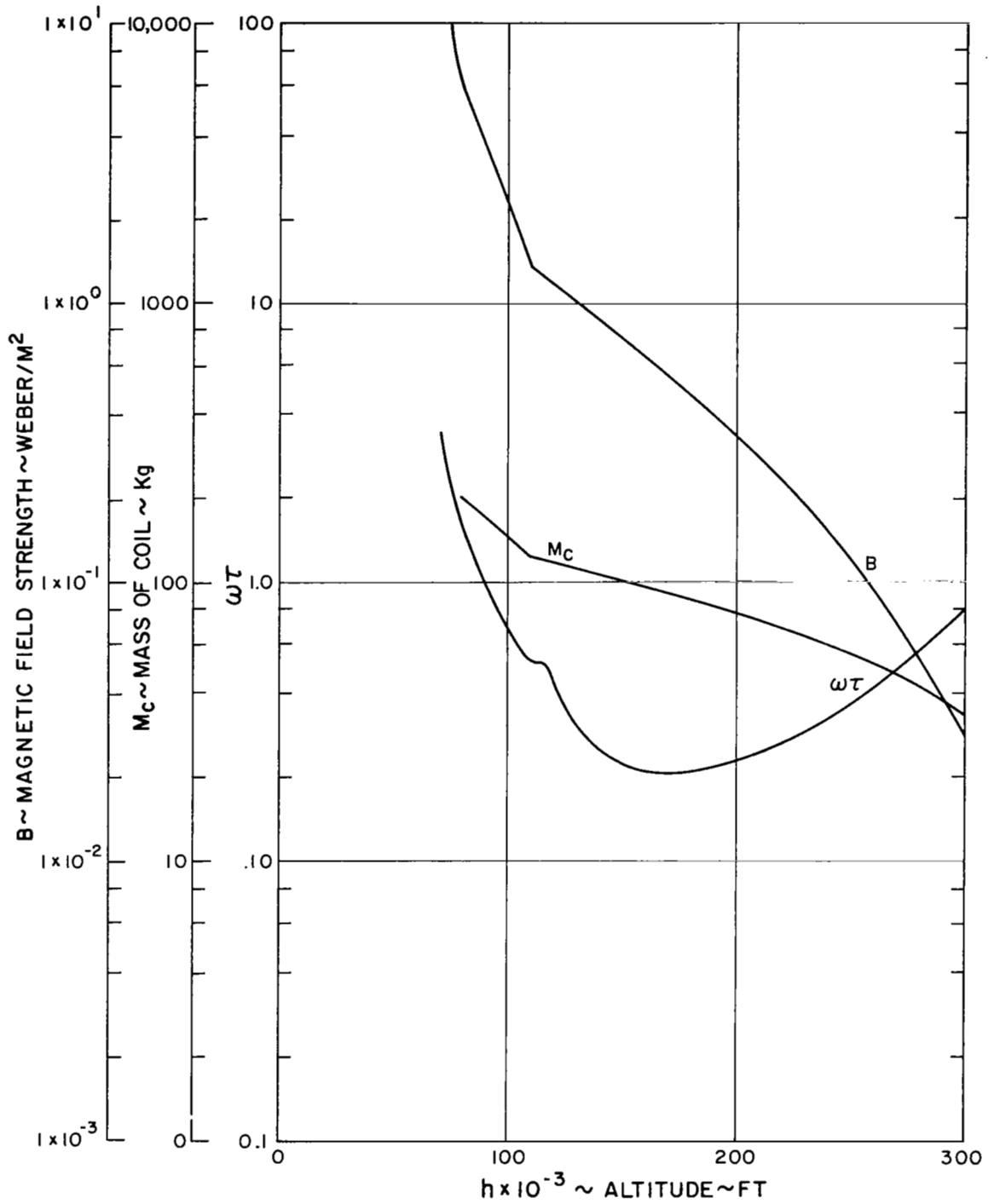


Fig. 7 Computer calculation of re-entry history  $B$ ,  $\omega\tau$ ,  $M_c$ ,  $V_E = 40,000$  ft/sec.

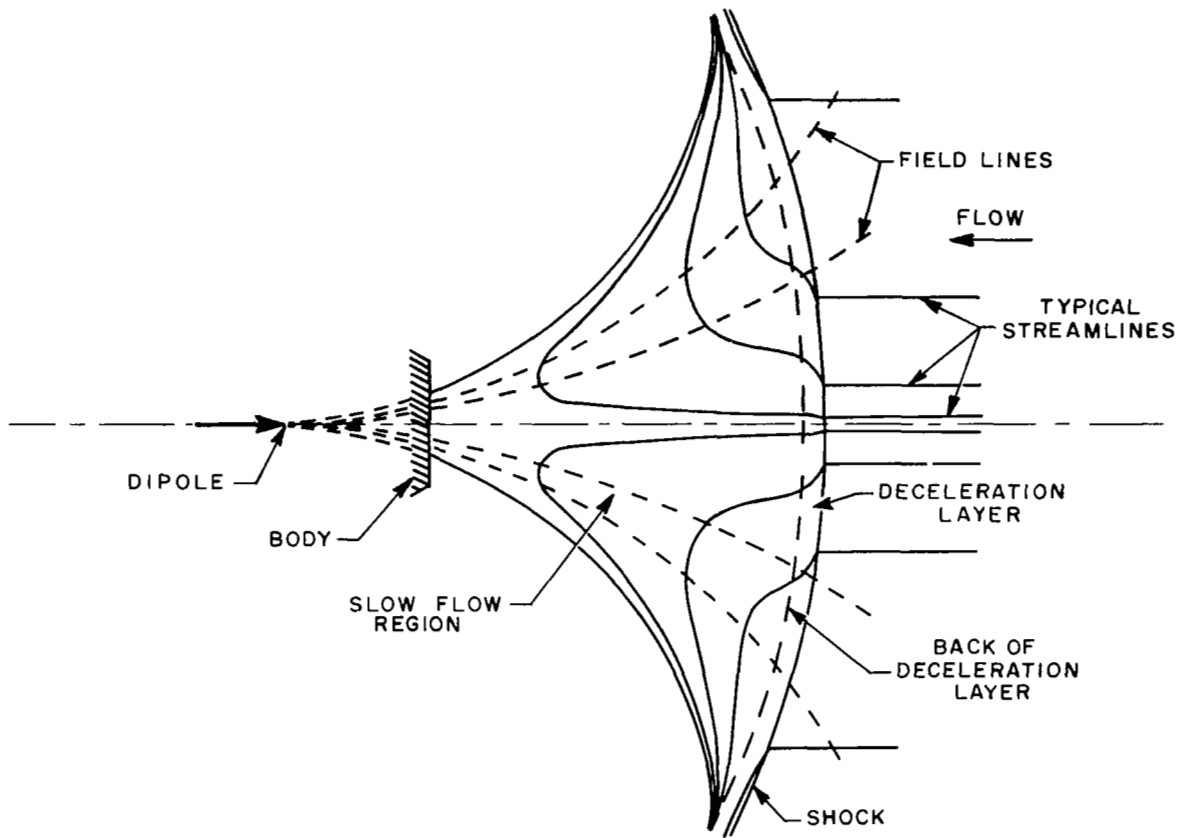
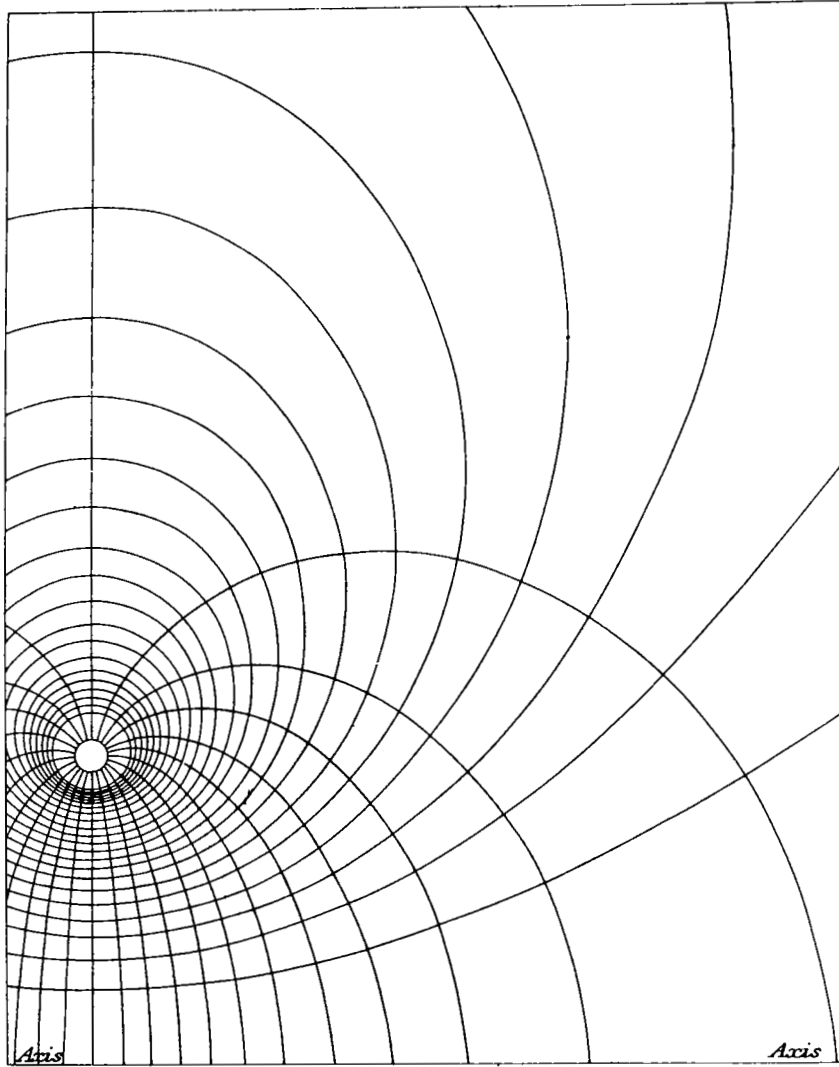


Fig. 8 Features of low  $R_M$  flow.



*Circular Current*

Fig. 9 Magnetic field lines of a circular current loop

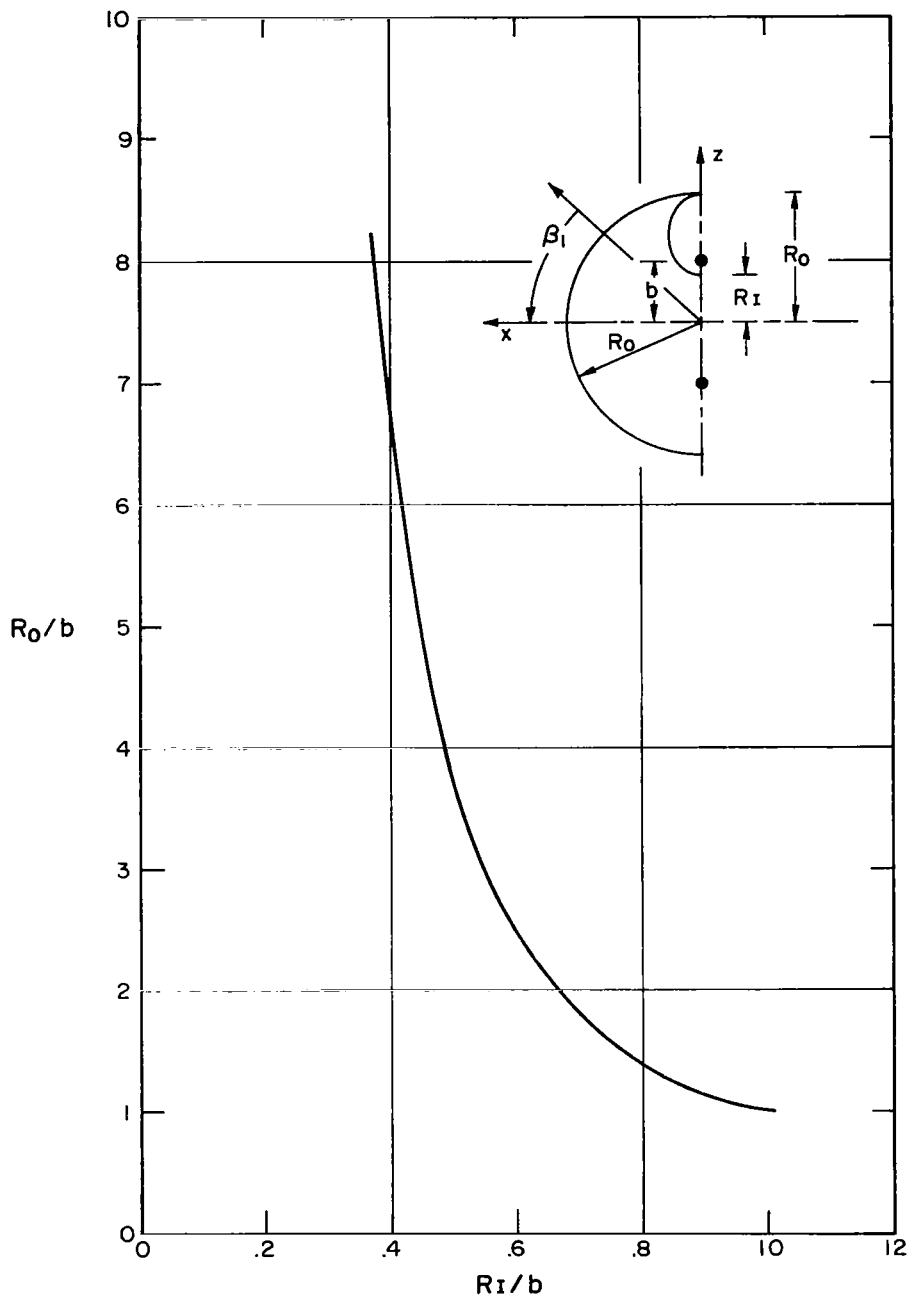


Fig. 10 Inner and outer locations of magnetic field lines  $\beta_1 = 90^\circ$ .

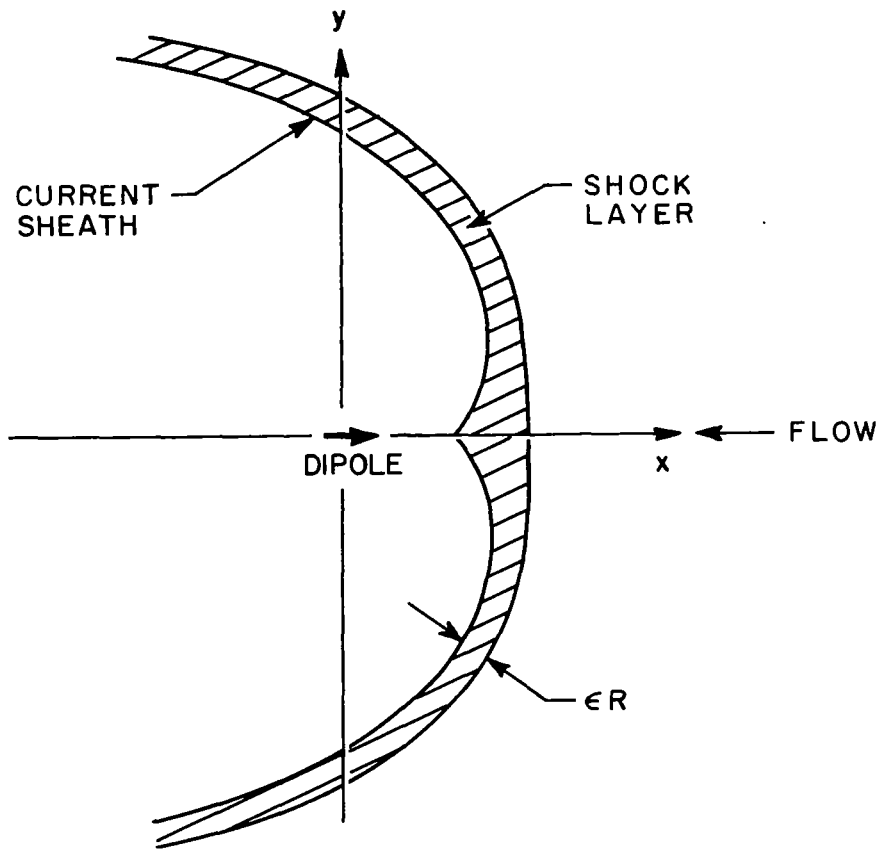


Fig. 11 Features of high  $R_M$  flow

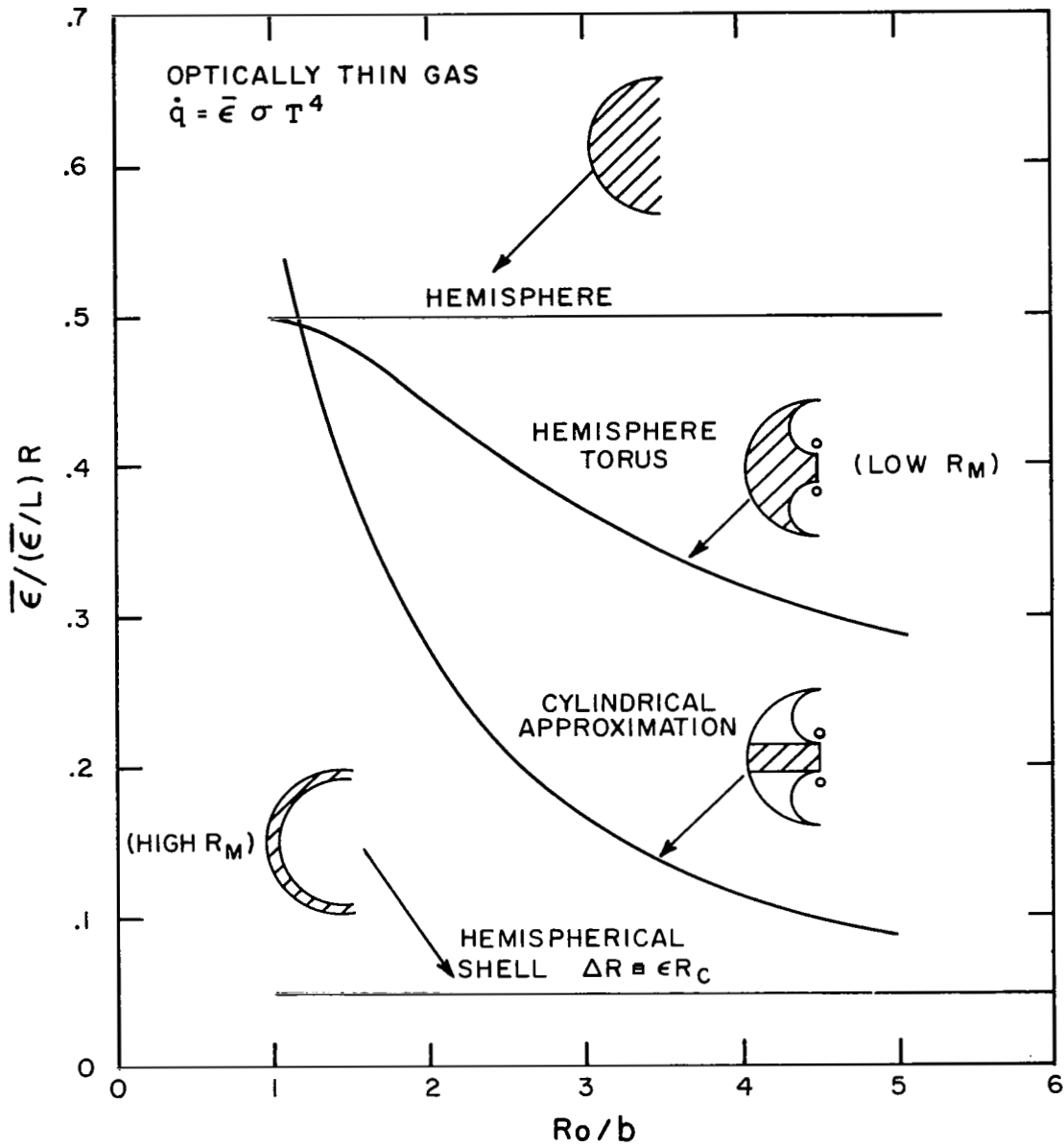


Fig. 12 Hemispherical emissivities of low  $R_M$  and high  $R_M$  gas volumes.

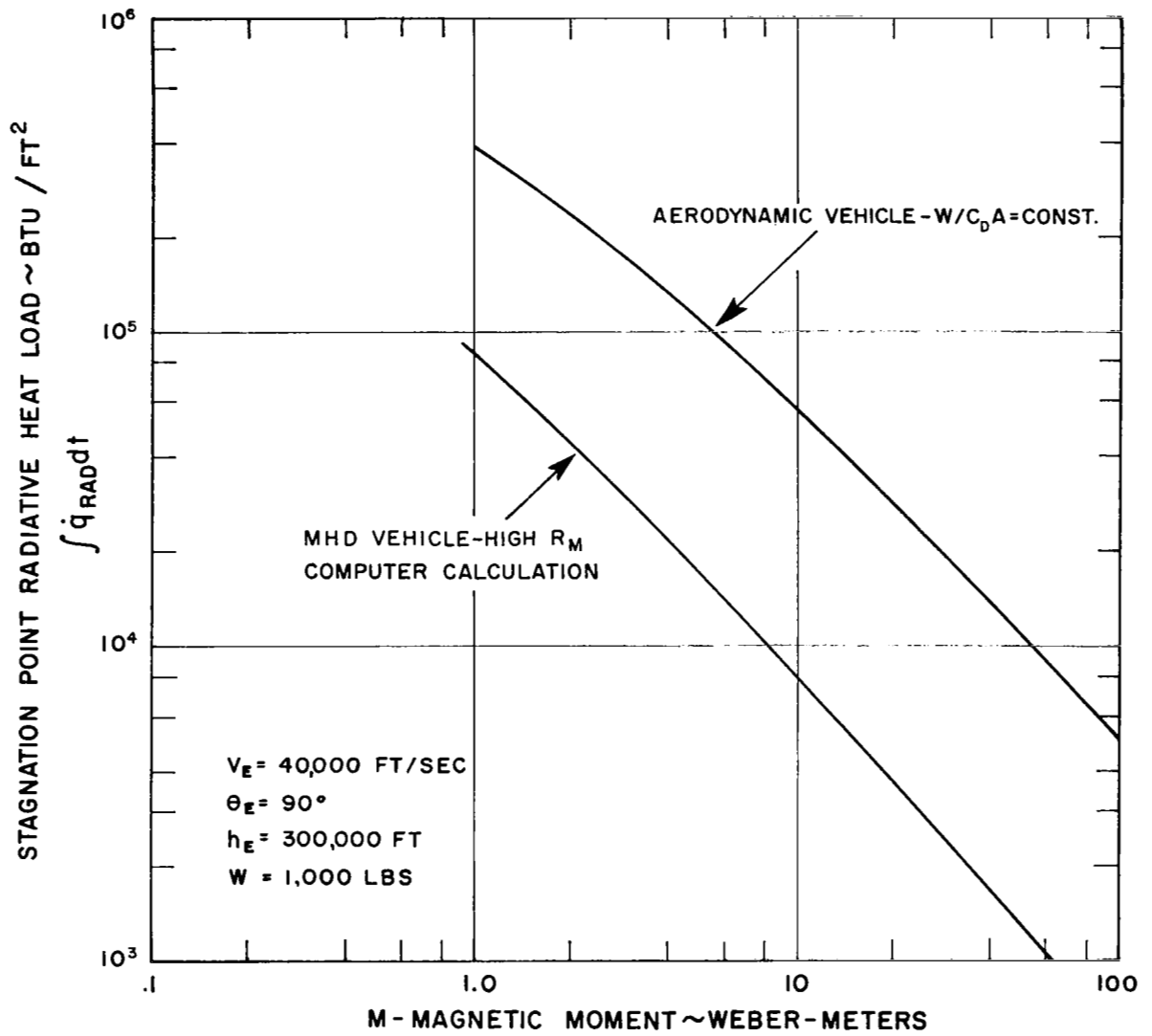


Fig. 13 Stagnation point radiative heat load-vertical re-entry  $V = 40,000$  ft/sec.

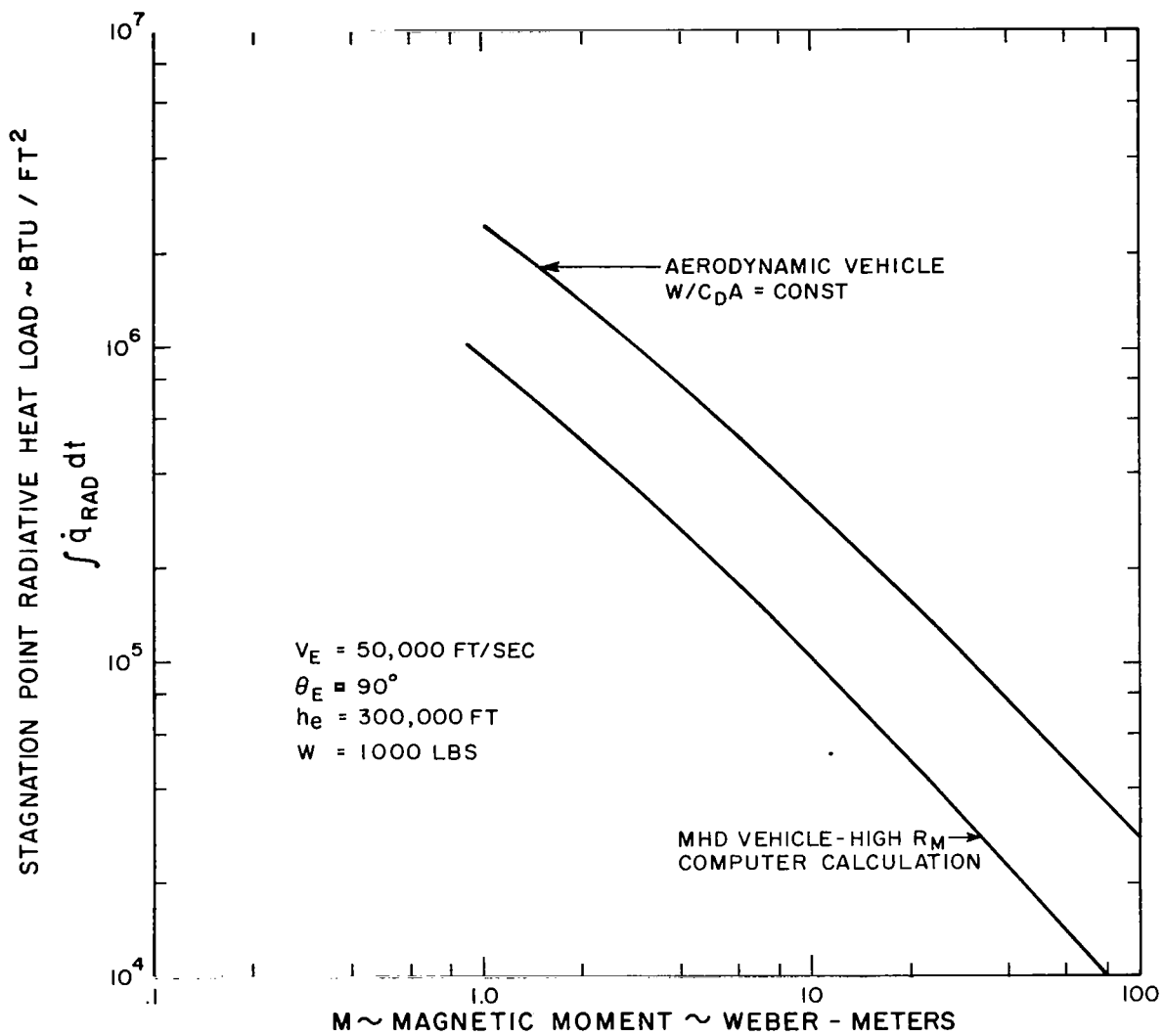


Fig. 14 Stagnation point radiative heat load-vertical re-entry  $V = 50,000$  ft/sec.

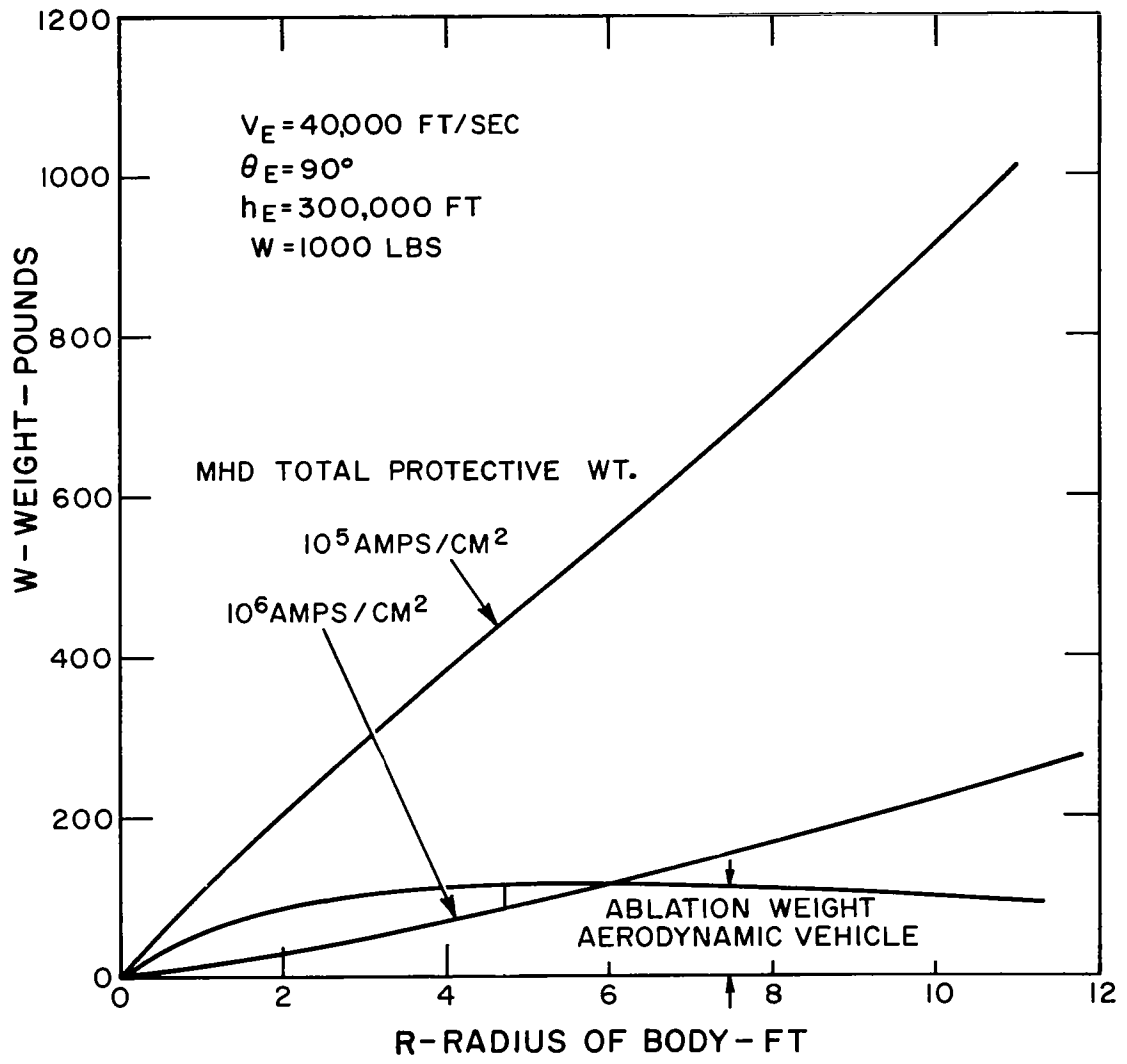


Fig. 15 Re-entry heating protective weight  $V = 40,000 \text{ ft/sec}$ .

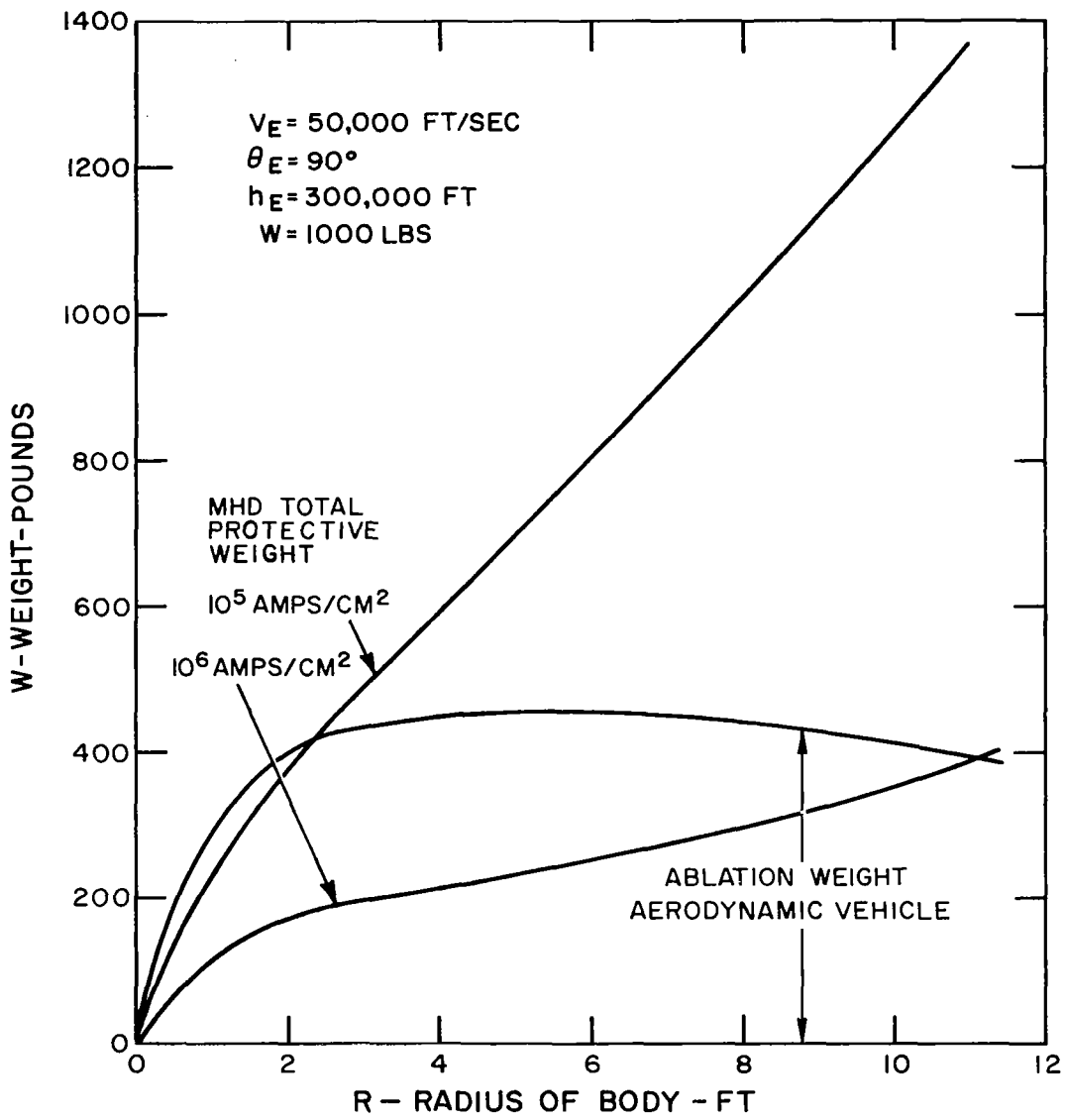


Fig. 16 Re-entry heating protective weight  $V = 50,000 \text{ ft/sec}$ .

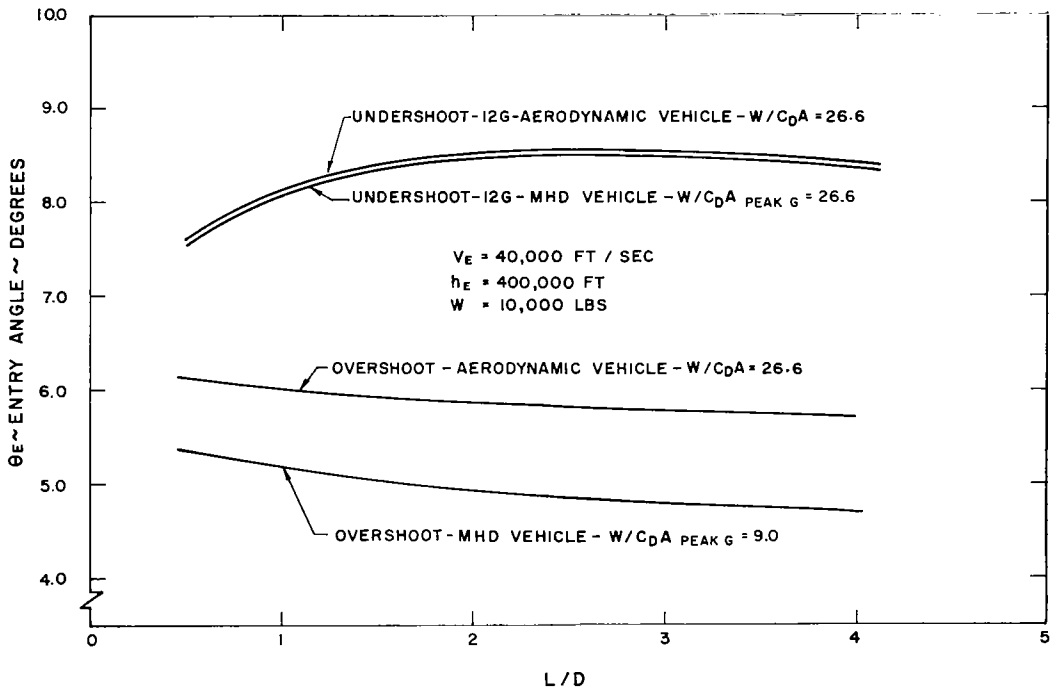


Fig. 17 Lifting re-entry - overshoot and undershoot boundaries.

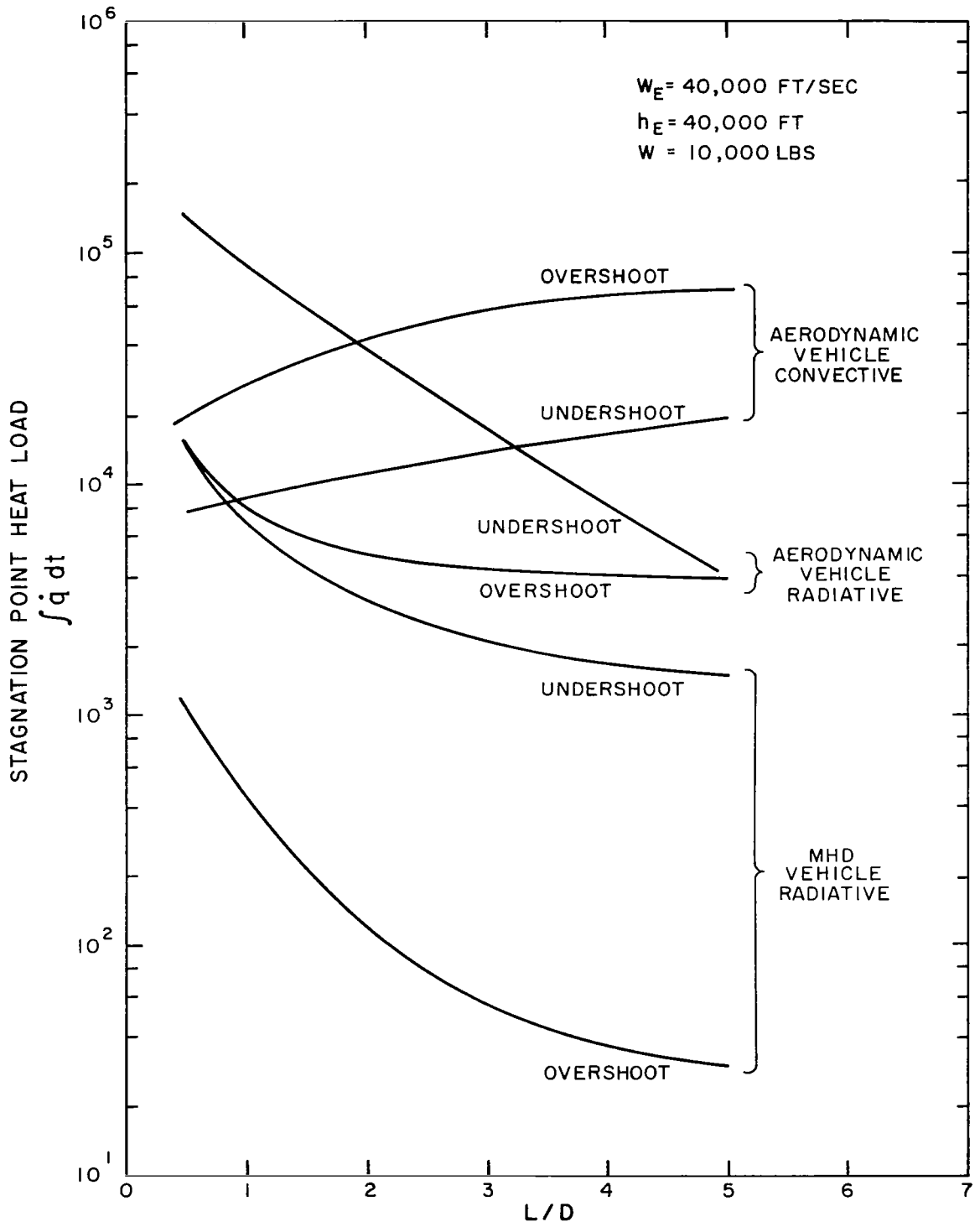


Fig. 18 Lifting re-entry - stagnation point heat load.

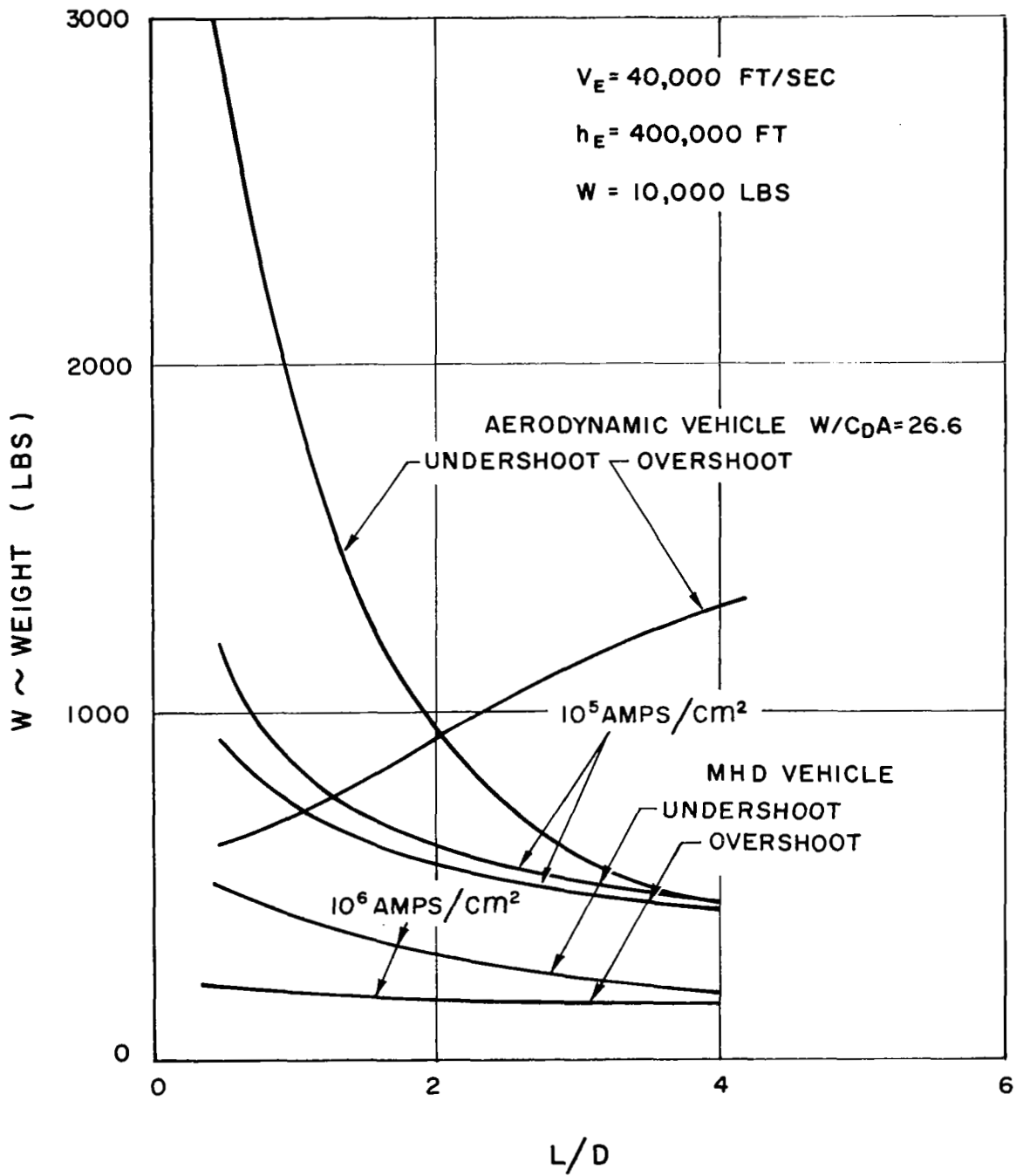


Fig. 19 Lifting re-entry - heating protective weight.

## APPENDIX A

### EMISSIVITY OF LOW $R_M$ GAS VOLUME

When a monochromatic beam has an intensity  $B_\lambda$  after having traveled a distance  $S$  in an absorbing gas, then the amount of  $dB_\lambda$  by which the intensity decreases through absorption on the next path length  $dS$  is described by the equation

$$\frac{dB_\lambda}{B_\lambda} = -a_\lambda dS \quad (\text{A-1})$$

The exponent  $a_\lambda$  is called the absorption coefficient. The preceding equation can be integrated when the temperature is constant. The result is  $B_\lambda = B_{\lambda_0} e^{-a_\lambda S}$ , where  $B_{\lambda_0}$  indicates the intensity with which the radiant beam enters the gas ( $S = 0$ ).

The transmissivity of a gas layer of thickness  $S$  is

$$\tau_\lambda = e^{-a_\lambda S} \quad (\text{A-2})$$

and the absorptivity is

$$\alpha_\lambda = 1 - e^{-a_\lambda S} \quad (\text{A-3})$$

Equation 3 also gives the emissivity  $\epsilon$  according to Kirchhoff's law,

$$\bar{\epsilon}_\lambda = 1 - e^{-a_\lambda S} \quad (\text{A-4})$$

Equation (A-1) is concerned with radiation traveling through the gas in a certain direction. When the absorptivity is set equal to the emissivity Eq. (A-4) has to be interpreted as the ratio of intensities

$$\bar{\epsilon}_\lambda = \frac{i_\lambda}{i_{b_\lambda}} = 1 - e^{-a_\lambda S} \quad (\text{A-5})$$

where  $i_\lambda$  equals the monochromator radiation intensity; and  $i_{b\lambda}$  equals the monochromator radiation intensity of a black body.

In calculations on heat exchange by radiation, one is primarily interested in the energy flux which arrives at a certain location  $dA$  on the boundary of the gas body and which comes from all directions in space. The radiative flux arriving per unit area and time, the emissive power, is given by

$$e_\lambda = \int i_\lambda d\omega \quad (A-6)$$

where  $d\omega$  indicates a small solid angle.

For a spherical coordinate system with its origin at  $dA$ , the solid angle  $d\omega$  can be expressed by two angles  $\beta$  and  $\phi$ . When additionally Eq. (A-5) is introduced, then the emissive power can be written

$$e_\lambda = \int_{\phi=0}^{\phi=2\pi} \int_{\beta=0}^{\beta=\pi/2} (1 - e^{-a_\lambda s}) i_{b\lambda} \sin \beta, d\beta, d\phi \quad (A-7)$$

One can define a hemispheric emissivity as the ratio of the emissive power  $e$  to the emissive power of a black surface at the same temperature.

$$\bar{\epsilon}_\lambda = \frac{e_\lambda}{e_{b\lambda}} = \frac{1}{\pi} \int_{\phi=0}^{\phi=2\pi} \int_{\beta=0}^{\beta=\pi/2} (1 - e^{-a_\lambda s}) \sin \beta, \cos \beta, d\beta, d\phi \quad (A-8)$$

This equation can be interpreted for a specific shape of radiating gas body.

If the self absorption of the gas is negligibly small, Eq. (A-8) becomes after expansion in a series

$$\bar{\epsilon}_\lambda = \frac{e_\lambda}{e_{b\lambda}} = \frac{1}{\pi} \int_{\phi=0}^{\phi=2\pi} \int_{\beta=0}^{\beta=\pi/2} a_\lambda s \sin \beta, \cos \beta, d\beta, d\phi \quad (A-9)$$

The preceding equations describe the total emissivity if the subscript  $\lambda$  is dropped and  $a$  is now considered to be the frequency averaged absorption coefficient. In the work to follow, the emissivity per unit length of high temperature air is obtained from Ref. 16 and is related to the absorption coefficient

$$\left(\frac{\bar{\epsilon}}{L}\right) = 2a \quad (\text{A-10})$$

This relationship is shown to be true in Refs. 17 and 18.

The hemispherical emissivity for a gas volume with the shape of a hemisphere radiating into the center of its base area can be found by integration of Eq. A-8. The integration over the angle  $\phi$  can be carried out immediately because of the rotational symmetry of the configuration. The path length  $S$  is in this case equal to the radius  $r$  of the hemisphere and is independent of angle

$$\bar{\epsilon}_H = 2 \int_0^{\pi/2} \left(1 - e^{-\frac{(\bar{\epsilon})R}{2}}\right) \cos\beta_1 d(\cos\beta_1) \quad (\text{A-11})$$

$$\bar{\epsilon}_H = \left(1 - e^{-\frac{(\bar{\epsilon})R}{2}}\right) \quad (\text{A-12})$$

For optically thin gas

$$\bar{\epsilon}_H = \frac{(\bar{\epsilon})R}{2}$$

Therefore, the total radiation per unit area to an area in the center of the base of the hemisphere for transparent gas is

$$\dot{q}_{\text{RAD}} = \left(\frac{\bar{\epsilon}}{L}\right) \sigma T^4 R/2 \quad (\text{A-14})$$

For optically thin gas, the emissivity of the low RM gas volume can be determined by taking the difference between the emissivity of a hemisphere and the emissivity of the toroid for semi-circular cross-section.

The geometry of the torus is shown in Fig. 1A. In a polar coordinate system, the equation of the torus is

$$(r-l)^2 + z^2 = R_1^2 \quad (\text{A-15})$$

In cartesian coordinate system, the equation of the torus is

$$x^2 + y^2 - 2\sqrt{x^2+y^2}l + l^2 + z^2 - R_1^2 = 0 \quad (\text{A-16})$$

In order to calculate the emissivity of the toroidal gas volume, the length  $\Delta S$  must be known as a function of  $\beta_1$ . The coordinates of the points of intersection of the line  $S$  and toroid are

$$\begin{aligned} X &= S \sin \beta_1 \cos \phi \\ Y &= -S \sin \beta_1 \sin \phi \\ Z &= S \cos \beta_1 \end{aligned} \quad (\text{A-17})$$

If the coordinates of Eq. (A-17) are substituted into the equation of the torus and the roots  $S$  of the equation are determined, it can be shown that

$$\Delta S = 2 \sqrt{l^2 \sin^2 \beta_1 - [r^2 - R_1^2]} \quad (\text{A-18})$$

where  $l = R_{\text{I}} + \frac{R_0 - R_{\text{I}}}{2}$  (A-19)

$$R_{\text{I}} = \frac{R_0 - R_{\text{I}}}{2} \quad (\text{A-20})$$

The angle at the point of tangency of the line from the center and the torus is

$$\beta_1^* = \pi/2 - \text{TAN}^{-1} \left( \frac{R_{\text{I}}}{\sqrt{l^2 - R_1^2}} \right) \quad (\text{A-21})$$

The emissivity of the toroid is then determined as follows:

$$\frac{\bar{\epsilon} \pi}{(\bar{\epsilon}) R} = \frac{\bar{\epsilon} \pi}{(\bar{\epsilon}) b} \frac{b}{R} \quad (\text{A-22})$$

$$\left( \frac{\bar{\epsilon}}{L} \right) R = \frac{b}{R} \left\{ \frac{1}{\pi} \int_{\phi=0}^{\phi=\pi} \int_{\beta_1=\beta_1^*}^{\beta_1=\pi/2} \left( \frac{\Delta S}{b} \right) \sin \beta_1 \cos \beta_1 d\beta_1 d\phi \right\} \quad (\text{A-23})$$

$$\text{where } \beta_1^* = \pi/2 - \tan^{-1} \left( \frac{R_2/b}{\sqrt{(l/b)^2 - (R_2/b)^2}} \right) \quad (\text{A-24})$$

$$\frac{\Delta S}{b} = 2 \sqrt{\left(\frac{l}{b}\right)^2 \sin^2 \beta_1 - \left[\left(\frac{l}{b}\right)^2 - \left(\frac{R_2}{b}\right)^2\right]} \quad (\text{A-25})$$

$$\frac{l}{b} = \frac{R_I}{b} + \frac{R_0/b - R_I/b}{2} \quad (\text{A-26})$$

$$\frac{R_2}{b} = \frac{R_0/b - R_I/b}{2} \quad (\text{A-27})$$

Equations (A-22) through (A-27) were then solved on the electronic computer using the variation of  $R_0/b$  and  $R_I/b$  shown in Fig. 14. The emissivity shown in Fig. 17 is then the difference between the emissivities of the hemispherical gas volume and the toroidal gas volume of semi-circular cross-section.

In self absorption by the gas must be considered the emissivity of the gas volume between the shock wave and the limiting field line is obtained by solution of the following integral

$$\begin{aligned} \bar{\epsilon} = & \frac{1}{\pi} \int_{\phi=0}^{\phi=2\pi} \int_{\beta_1=0}^{\beta_1=\beta_1^*} \left(1 - e^{-\left(\frac{\bar{\epsilon}}{L}\right)R/2}\right) \sin \beta_1 \cos \beta_1 d\beta_1 d\phi \\ & + \frac{1}{\pi} \int_{\phi=C}^{\phi=2\pi} \int_{\beta_1=\beta_1^*}^{\beta_1=\pi/2} \left(1 - e^{-\left(\frac{\bar{\epsilon}}{L}\right)\delta/2}\right) \sin \beta_1 \cos \beta_1 d\beta_1 d\phi \end{aligned}$$

$$\begin{aligned} \text{WHERE } S &= R - \Delta S \\ &= R - 2 \sqrt{l^2 \sin^2 \beta_1 - [l^2 - R_2^2]} \end{aligned}$$

The variation of radiation of a hemispherical gas body to an area on its base as that area is moved radially outward is shown in Fig. 2(a)

for an optically thin gas. The distance  $x_0$  is the distance of the area  $dA$  from the center of the base of the hemisphere. The heat radiated to a unit area at the edge of the sphere is 40 percent of that radiated to an area in the center of the base of the hemisphere. The radiation of the low  $R_M$  gas volume to an area at various radial positions has also been calculated for an optically thin gas Fig. 3(a). The emissivity for Fig. 3(a) has been divided by the emissivity per unit length and the radius of the magnetic coil  $b$  to form the ratio  $\bar{\epsilon}/(\bar{\epsilon}/L)b$

The emissivity of a hemispherical body may be placed on Fig. 3(a) by recognizing that

$$\frac{\bar{\epsilon}_H}{(\bar{\epsilon}/L)b} = \frac{\bar{\epsilon}_H}{(\bar{\epsilon}/L)R} \frac{R}{b}$$

and that

$$R/b = R/R_0 \frac{R_0}{b}$$

This comparison is shown in Fig. 4(a) for the region  $0 < R/b < 1.0$ . At  $R/b = 1.0$  and  $R_0/R = 5.0$  the radiative heating due to low  $R_M$  gas volume is approximately forty percent of the radiative transfer by the hemispherical gas volume.

## APPENDIX B

### CYLINDRICAL APPROXIMATION TO LOW $R_M$ GAS VOLUME

The low  $R_M$  gas volume is approximated by a cylinder with radius equal to the radius of the inner field line and height equal to the outer radius of the same field line (Fig. 1(b)). The radiation of a cylindrical gas body to an area in the center of its base including self-absorption was treated by E. Schmidt (1933) and is reproduced in Ref. 11. In the present notation

$$\bar{\epsilon} = \frac{1}{\pi} \int_{\phi=0}^{\phi=2\pi} \int_{\beta_1=0}^{\beta_1=\tan^{-1}\left(\frac{R_I}{R_0}\right)} \left(1 - e^{-\left(\frac{\bar{\epsilon}}{L}\right) R_0 / 2 \cos \beta_1}\right) \sin \beta_1 \cos \beta_1 d\beta_1 d\phi$$

$$+ \frac{1}{\pi} \int_{\phi=0}^{\phi=2\pi} \int_{\beta_1=\tan^{-1}\left(\frac{R_I}{R_0}\right)}^{\beta_1=\pi/2} \left(1 - e^{-\left(\frac{\bar{\epsilon}}{L}\right) R_I / 2 \sin \beta_1}\right) \sin \beta_1 \cos \beta_1 d\beta_1 d\phi$$

For an optically thin gas and carrying the integration over the angle  $\phi$  because of the rotational symmetry of the configuration.

$$\bar{\epsilon} = \left(\frac{\bar{\epsilon}}{L}\right) R_0 \int_{\beta_1=0}^{\beta_1=\tan^{-1}\left(\frac{R_I}{R_0}\right)} \sin \beta_1 d\beta_1$$

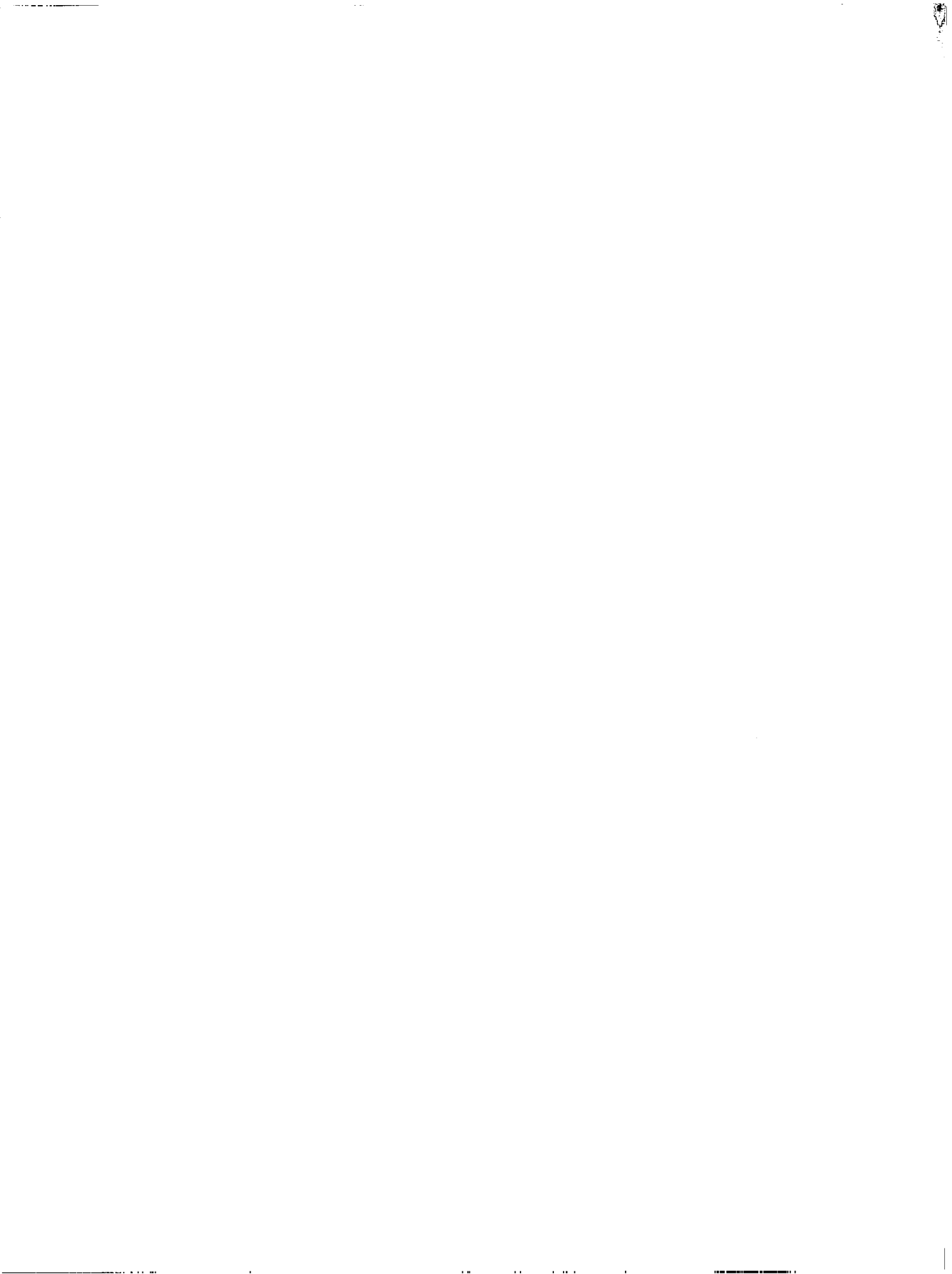
$$+ \left(\frac{\bar{\epsilon}}{L}\right) R_I \int_{\beta_1=\tan^{-1}\left(\frac{R_I}{R_0}\right)}^{\beta_1=\pi/2} \cos \beta_1 d\beta_1$$

which reduces to

$$\frac{\bar{\epsilon}}{\left(\frac{\bar{\epsilon}}{L}\right) R_0} = \left(1 - \cos \left[ \tan^{-1} \left( \frac{R_I}{R_0} \right) \right] \right)$$

$$+ \frac{R_I}{R_0} \left(1 - \sin \left[ \tan^{-1} \left( \frac{R_I}{R_0} \right) \right] \right)$$

This expression was evaluated using the variation of  $R_I$  and  $R_0$  (Fig. 10) and is presented in Fig. 12.



## APPENDIX C

### EMISSIVITY OF HEMISPHERICAL SHELL VOLUME

The emissivity  $\epsilon$  for the hemispherical shell volume is determined by evaluating

$$\bar{\epsilon} = \frac{1}{\pi} \int_{\phi=0}^{\phi=2\pi} \int_{\beta_1=0}^{\beta_1=\pi/2} \left( 1 - e^{-\frac{(\bar{\epsilon})S}{2}} \right) \sin \beta_1 \cos \beta_1 d\beta_1 d\phi \quad (C-1)$$

The integration over the angle  $\phi$  can be carried out immediately because of the rotational symmetry of the configuration. For hemispherical shell the path length  $S$  is equal to the shell thickness  $\Delta R = \epsilon R$  and is therefore independent of angle

$$\bar{\epsilon} = \left( 1 - e^{-\left(\frac{\bar{\epsilon}}{L}\right) \Delta R/2} \right) = \left( 1 - e^{-\left(\frac{\bar{\epsilon}}{L}\right) \epsilon R/2} \right) \quad (C-2)$$

For optically thin gas, the emissivity of the shell volume is

$$\frac{\bar{\epsilon}}{\left(\frac{\bar{\epsilon}}{L}\right) R} = \epsilon/2 \quad (C-3)$$

Assuming a nominal value of 1/10 for the density ratio  $\epsilon$

$$\frac{\bar{\epsilon}}{\left(\frac{\bar{\epsilon}}{L}\right) R} \approx \frac{1}{20} \quad (C-4)$$

The radiative heating due to the hemispherical shell of gas is therefore 1/10 that of the hemispherical gas body. (See Eq. A-14)



## APPENDIX D

### RADIATION HEATING MODEL FOR AERODYNAMIC VEHICLE

The geometry of the radiating gas volume for the aerodynamic vehicle is shown in Fig. 1(d). The radius of curvature of the heat shield of the aerodynamic vehicle is twice the radius of the vehicle. The shock stand-off distance is equal to the density ratio  $\epsilon$  across the shock times the radius of curvature

$$\delta = \epsilon R_c = 2 \epsilon R \quad (D-1)$$

For purposes of radiation calculation, the slightly curved gas volume is approximated by a circular cylinder of radius  $R$  and depth  $2\epsilon R$  (Fig. 1D). The emissivity of the circular cylindrical gas volume can be calculated by the method previously described in Appendix B.

$$\begin{aligned} \bar{\epsilon} = & 2 \int_{\beta_1=0}^{\beta_1=\text{TAN}^{-1}\left(\frac{1}{2\epsilon}\right)} \left( 1 - e^{-\left(\frac{\bar{\epsilon}}{L}\right) \epsilon R / \cos \beta_1} \right) \sin \beta_1 \cos \beta_1 d\beta_1, \quad (D-2) \\ & + 2 \int_{\beta_1=\text{TAN}^{-1}\left(\frac{1}{2\epsilon}\right)}^{\beta_1=\pi/2} \left( 1 - e^{-\left(\frac{\bar{\epsilon}}{L}\right) R / 2 \sin \beta_1} \right) \sin \beta_1 \cos \beta_1 d\beta_1, \end{aligned}$$

For an optically thin gas, Eq. (D-2) reduces to

$$\begin{aligned} \bar{\epsilon} = & 2 \left( \frac{\bar{\epsilon}}{L} \right) \epsilon R \int_{\beta_1=0}^{\beta_1=\text{TAN}^{-1}\left(\frac{1}{2\epsilon}\right)} \sin \beta_1 d\beta_1 \\ & + \left( \frac{\bar{\epsilon}}{L} \right) R \int_{\beta_1=\text{TAN}^{-1}\left(\frac{1}{2\epsilon}\right)}^{\beta_1=\pi/2} \cos \beta_1 d\beta_1 \end{aligned}$$

Performing the integrations

$$\frac{\bar{\epsilon}}{\left(\frac{\bar{\epsilon}}{L}\right)R} = \left[ 2\epsilon \left( 1 - \cos \left[ \text{TAN}^{-1} \left( \frac{1}{2\epsilon} \right) \right] \right) + \left( 1 - \sin \left[ \text{TAN}^{-1} \left( \frac{1}{2\epsilon} \right) \right] \right) \right]$$

Assuming  $\epsilon$  is nominally 1/10

$$\begin{aligned} \text{TAN}^{-1} \left( \frac{1}{2\epsilon} \right) &= \text{TAN}^{-1}(5.0) \\ &= 78.7^\circ \end{aligned}$$

AND

$$\frac{\bar{\epsilon}}{\left(\frac{\bar{\epsilon}}{L}\right)R} = .18$$

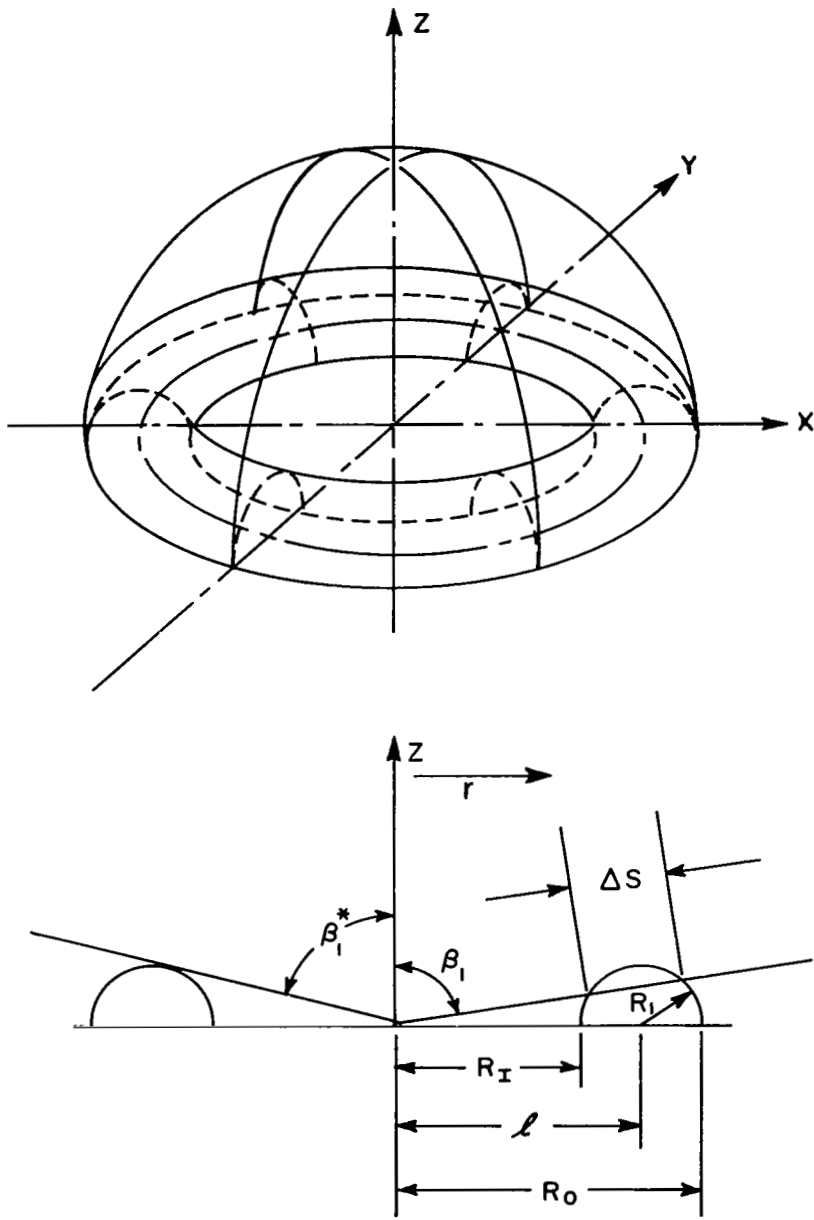


Fig. 1A Geometry of Low  $R_M$  Gas Volume.

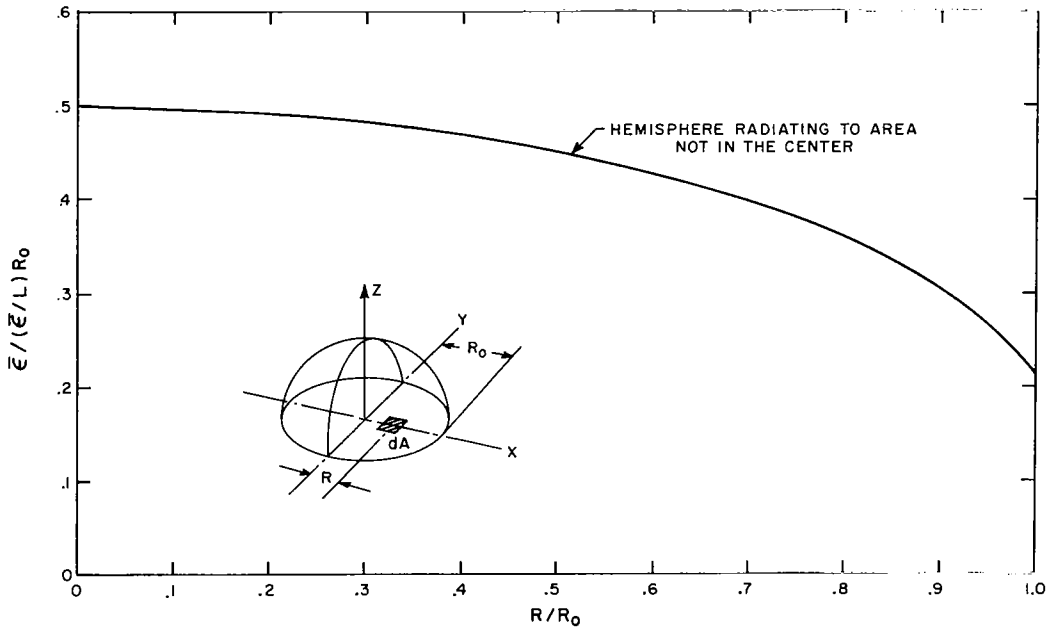


Fig. 2A Radiation Heating of Hemispherical Gas Volume to an Area not in the Center of its Base.

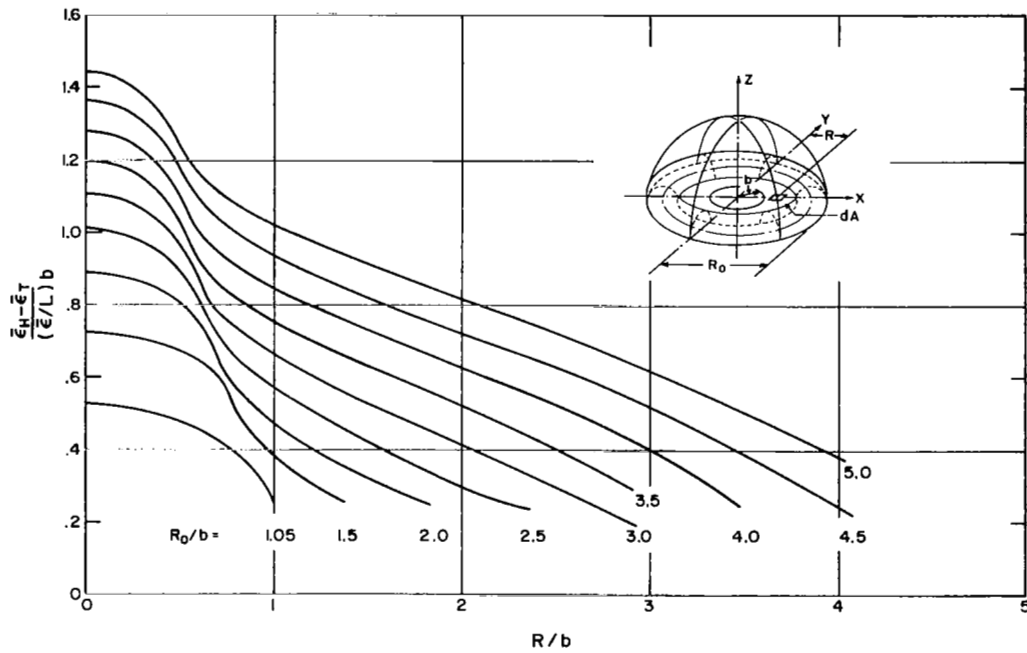


Fig. 3A Radiation Heating of Low  $R_M$  Gas Volume to an Area not in the Center of its Base.

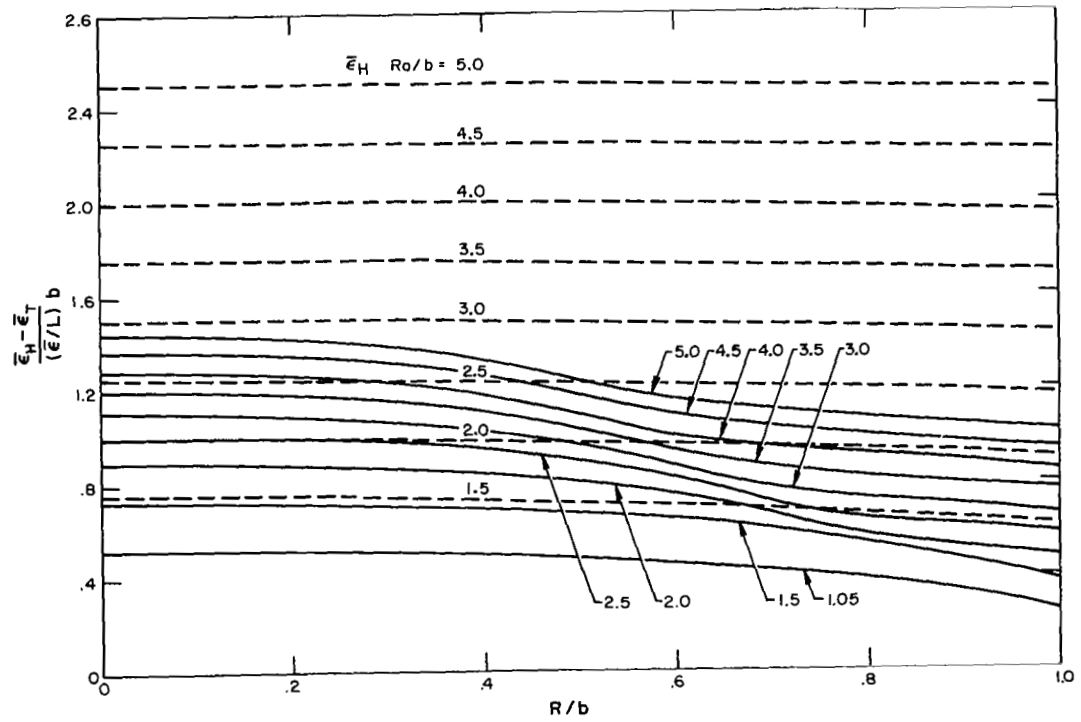


Fig. 4A Radiation Heating of Low  $R_M$  Gas Volume  $0 \leq R/b \leq 1.0$ .

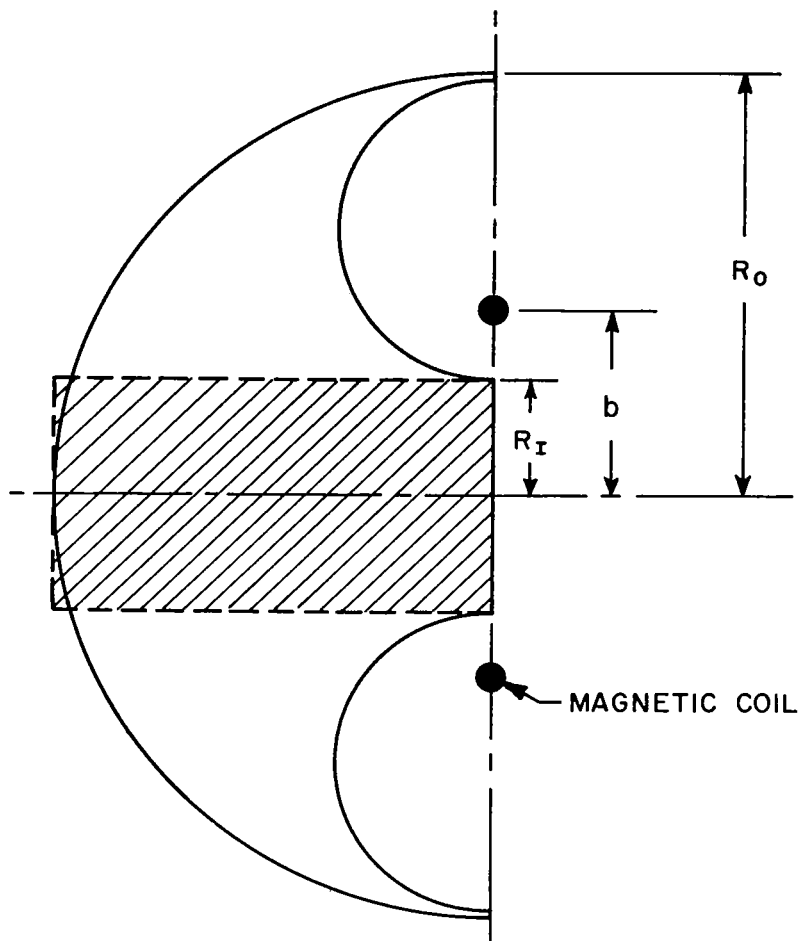


Fig. 1B Geometry of Cylindrical Approximation to Low  $R_M$  Gas Volume.

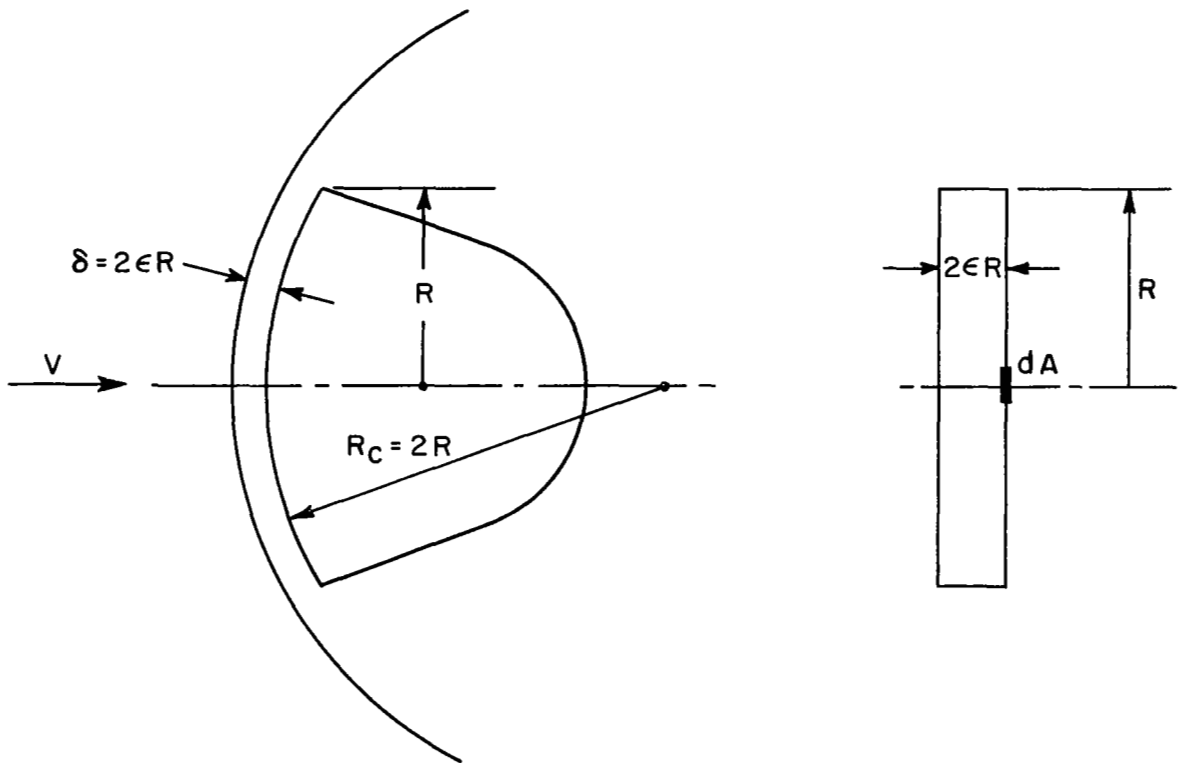


Fig. 1D Geometry of Aerodynamic Vehicle's Radiating Gas Volume.

## REFERENCES

1. Kantrowitz, A. R., "Flight Magnetohydrodynamics," Avco-Everett Research Laboratory Research Report 51, March 1959.
2. Levy, R. H. and Petschek, H. E., "The Magnetohydrodynamically Supported Hypersonic Shock Layer," Avco-Everett Research Laboratory Research Report 140, September 1962.
3. Locke, E. V., Petschek, H. E. and Rose, P. H., "The Magnetohydrodynamically-Supported Hypersonic Shock Layer. Part II - Experimental," Fourth Symposium on the Engineering Aspects of Magnetohydrodynamics. University of California, Berkeley, California, April 10-11, 1963.
4. Levy, R. H., "Interaction of a Streaming Plasma with the Magnetic Field of a Two-Dimensional Dipole," Avco-Everett Research Laboratory Research Report 159, August 1963.
5. Levy, R. H., Gierasch, P. J., and Henderson, D. B., "Hypersonic Magnetohydrodynamics with or without a Blunt Body," Avco-Everett Research Laboratory Research Report 173, January 1964.
6. Allen, H. J., and Eggers, A. J., Jr., "A Study of the Motion and Aerodynamic Heating of Missiles Entering the Earth's Atmosphere at High Supersonic Speeds," Ames Aeronautical Laboratory, Moffett Field, California, NACA TN4047.
7. Stekly, Z. J. J., "Magnetic Energy Storage using Superconducting Coils," Avco-Everett Research Laboratory AMP 102, January 1963.
8. Stekly, Z. J. J., "The Feasibility of Large Superconducting Coils," Avco-Everett Research Laboratory Research Report 160, September 1963.
9. Lees, L., Hartwig, F. W. and Cohen, O. B., "The Use of Aerodynamic Lift During Entry into the Earth's Atmosphere." Paper presented at the ARS Controllable Satellites Conference, Massachusetts Institute of Technology, April 30, 1959.
10. Teare, J. D., "Ionization Behind Shock Waves," Volume 12, Ions and Electrons In Combustion Systems, Progress in Astronautics and Rocketry Series.

11. Eckert, E. R. G. and Drake, R. M., Jr., "Heat and Mass Transfer," McGraw-Hill Book Company 1959.
12. Maxwell, J. C., "A Treatise On Electricity and Magnetism." Reproduction Of The Third Edition 1891 Dover Publications Inc., 1954.
13. Hurley, J., Physics of Fluids 9, 854, (1961).
14. Dungey, J. W., Pennsylvania State University, Sci. Rept. No. 135 (1960)
15. Zhiguliv, V. V. and Romishevski, E. A., Soviet Physics - Doklady 4, 859 (1960).
16. Kivel, B. and Bailey, K., "Tables of Radiation from High Temperature Air," Avco-Everett Research Laboratory Research Report 21, December 1957.
17. Kivel, B., "Radiation from Hot Air and Stagnation Heating." Avco-Everett Research Laboratory Research Report 79, October 1959.
18. Goulard, R., "Fluxes and Non-Dimensional Parameters in Radiant Gases," Purdue University Report No. A-59-8, October 1959.
19. Levy, R. H., "Author's Reply to Willinskis Comment on "Radiation Shielding of Space Vehicles by Means of Superconducting Coils," ARS Journal May 1962, p. 787.
20. Pritchard, E. Brian, "Survey of Velocity Requirements and Re-entry Flight Mechanics for Manned Mars Missions," Aerospace Sciences Preprint 64-13 (1964).
21. Chapman, D. R., "An Analysis of the Corridor and Guidance Requirements for Supercircular Entry into Planetary Atmospheres," NASA Technical Report R-55.
22. Fishman, F., Lothrop, J., Patrick, R. and Petschek, H., "Supersonic Two-Dimensional Magnetohydrodynamic Flow," Avco-Everett Research Laboratory Research Report 39 (1958).
23. Kemp, N. H. and Riddell, F. R., "Heat Transfer to Satellite Vehicles Re-entering the Atmosphere," Avco-Everett Research Laboratory Research Report 2 (1956).
24. Fay, J. A. and Riddell, F. R., "Theory of Stagnation Point Heat Transfer in Dissociated Air," Avco-Everett Research Laboratory Research Report 1 (1958).